FATE OF DISSOLVED ORGANIC MATTER ALONG THE SUPRA-PERMAFROST FLOW: ROLE OF ARCTIC SUBTERRANEAN ESTUARIES

Aude Flamand[1] (ORCID : 0000-0001-9983-4176)

Jean-François Lapierre[2,3] (ORCID : 0000-0001-5862-7955)

Gwénaëlle Chaillou[1] (ORCID: 0000-0002-4170-8852)

[1] Québec-Océan, Institut des Sciences de la Mer de Rimouski, Université du Québec à Rimouski, 310 Allée des Ursulines, Rimouski, Québec, Canada, G5L 3AL.

[2] Département de sciences biologiques, Université de Montréal, 1375 Avenue Thérèse-Lavoie-Roux, Montréal, Québec, Canada, H2V 0B3.

[3] Groupe de Recherche Interuniversitaire en Limnologie (GRIL).

Corresponding Author: Gwénaëlle Chaillou. Email: gwenaelle_chaillou@uqar.ca

ABSTRACT

Increasing coastal erosion and permafrost thaw along the Arctic shoreline represent major lateral sources of dissolved organic matter (DOM) to the Arctic coastal ocean, where DOM fate depends on its composition and transport pathways. One key and still underseen transport mechanism is supra-permafrost groundwater flow that discharges through the sandy beach in front of the coastal bluffs. Here we explore the fate of DOM and DOC along the supra-permafrost flow, with a specific focus on the sandy beach area. To address this, we sampled meltwater, beach groundwater, and seawater along coastal bluff transects extending up to 1 km offshore. Along these salinity and redox gradients, we observed sharp declines in dissolved organic carbon (DOC) and chromophoric DOM (CDOM), indicating substantial removal. Optical indices (aCDOM350, SUVA254, HIX) and PARAFAC-based fluorescence analysis revealed a shift from humic-like, high molecular weight (HMW) DOM in meltwaters to protein-like, low molecular weight (LMW) DOM in nearshore adjacent waters. While amorphous reactive Fe-hydroxides primarily retained humic substances, the strong inverse correlation between humic and protein-like components, together with acidic pH, dissolved total Fe and elevated dissolved inorganic carbon (DIC) in beach groundwater, points to microbial degradation as a major driver of DOM transformation along the supra-permafrost flow path. Fe-addition experiments further confirmed rapid DOC and CDOM removal via interactions with reactive Fe-hydroxides. These findings underscore the role of nearshore and intertidal zones, particularly within subterranean estuaries, where supra-permafrost groundwater mixes with recirculated seawater, as important regulators of DOM composition and persistence, acting as transient or permanent carbon sinks during Arctic permafrost-to-ocean transfer.

KEYWORDS: permafrost, Arctic coastal ocean, dissolved organic matter, dissolved organic carbon, iron hydroxide.

1 INTRODUCTION

Permafrost stores around 1,300 Pg of organic carbon (OC) within its 13.9 × 10^6 km^2 surface area, which represents 60 % of the world's soil organic carbon stored in 15 % of global soil area(Obu et al. 2019; Schuur et al. 2015). The Arctic permafrost coastline is heavily impacted by global changes, causing unprecedented thawing rates and the deepening of the active layer, which, in turn, increases subsurface transport (Jones et al. 2020; Lantuit et al. 2012). Unlithified and ice-bonded permafrost cliffs, such as those along the Beaufort Sea, are highly susceptible to coastal erosion. Over the past twenty years, these cliffs have experienced one of the highest coastal erosion rates recorded in the Arctic, with a recorded rate of 1.1 m yr^{-1} between 1950 and 2000. This rate has increased by 80–160 % in the last two decades (Jones et al. 2020; Lantuit et al. 2012). Accelerating coastline erosion is supplying increasing quantities of terrestrial materials (Kipp et al. 2018), associated nutrients (e.g., nitrogen and phosphorus; Fritz et al. 2017), carbon (including organic carbon and methane; Bristol et al. 2021), and contaminants (as heavy metals and organic pollutants; Kwasigroch et al. 2018) to the nearshore and coastal ocean. Recent studies show that land-derived nutrients from coastal erosion support approximately ~30 to 50% of primary production in the Arctic Ocean, highlighting the critical biogeochemical role of permafrost-derived nutrient recycling on Arctic shelves (Terhaar et al., 2021; Vonk et al., 2025). These diffuse, non-point sources release solutes that are remobilized in late summer, when thaw depths and coastal hydraulic gradients peak (Walvoord & Striegl, 2007; Lecher, 2017).

Dissolved organic matter (DOM) represents a fundamental link between terrestrial and aquatic carbon cycles, playing a significant role in the biogeochemistry of aquatic ecosystems (Hedges & Keil 1995). At the ocean-basin scale, newly mobilized organic matter from Arctic watersheds may lead, among other things, to enhanced emissions of CO_2 or other greenhouse gases (Lapham et al., 2020; Tanski et al. 2019; Vonk et al. 2015, 2025; Kaiser et al. 2017) and modifications in the productivity of primary producers (Nguyen et al., 2022; McMeans et al. 2015; Thingstad et al. 2008) that sustain the marine Arctic food web, with unknown impacts on the communities that rely on these food sources. This new input affects ocean chemistry by altering carbon and nutrient cycling (Guo et al. 2007; Stedmon et al. 2011; Vonk et al. 2014) and changes optical conditions,

reducing light penetration and limiting primary production (Fichot et al. 2013; Matsuoka et al. 2012). A fraction of this terrestrial DOM can be rapidly mineralized through microbial and photochemical processes, affecting nutrient budgets, air-sea CO_2 exchanges, biological productivity, as well as acidification, in coastal waters (Kaiser et al. 2017a; Kaiser et al. 2017b). For example, Kaiser et al. (2017a) showed that ~50% of the annual DOC discharged by Siberian rivers was mineralized in estuaries and on Eurasian continental shelves, indicating significant removal before reaching the open ocean. Therefore, only a small fraction of terrestrially-derived compounds potentially persists in the ocean over centuries and millennia (Fichot & Benner 2014; Kaiser et al. 2017a). While the export of terrestrial dissolved organic carbon (tDOC) is known to significantly influence the Arctic marine ecosystem, with an estimated 25–38 Tg C per year discharged into the Arctic Ocean (Holmes et al., 2012), the role and significance of inputs from coastal erosion and permafrost thaw in shaping the biogeochemistry and ecology of nearshore Arctic waters remain poorly understood. This knowledge gap stems not only from the stochastic and episodic nature of erosion- and thaw-related fluxes, which complicates their quantification, but also from the complex interactions between mineral and organic phases that control the stabilization, transformation, and transport of tDOM along flow paths. The mechanisms of organic matter transformations occurring at mineral-organic interfaces are complex (see Li et al., 2023; and references therein), particularly in intertidal sandy sediment where biological, geochemical, and redox conditions interplay to influence DOM concentrations and molecular compositions. One key process in these dynamic transitional environments is the formation of iron (Fe) curtains at the redox interface, which may serve as major zones for the storage and transformation of terrigenous organic carbon (OC) (Amoako et al., 2025; Chen et al., 2014; Linkhorst et al., 2017; Sirois et al., 2018; Zhou et al., 2023, 2024).

Subterranean estuaries (STEs) are coastal aquifers where terrestrial groundwater mixes with recirculating seawater (Moore, 1999). These zones act as biogeochemical hotspots (Anschutz et al., 2009) with the iron (Fe) cycle playing a central role in both the remineralization and sequestration of organic matter (OM) (Charette & Sholkovitz, 2002; Sirois et al., 2018; Chaillou et al., 2024). Redox oscillations, driven by fluctuations in water levels (e.g., tides, waves, sea-level rise, and water table variations; Santos et al., 2012), control the zones where Fe precipitates as Fe-hydroxides. These so-called “iron curtains” function as transient or persistent geochemical

barriers, especially for elements with strong affinities to Fe-hydroxide surfaces, including dissolved organic matter (DOM), and thus modulate their export to adjacent coastal waters (Riedel et al., 2013; Linkhorst et al., 2017; Sirois et al., 2018; Waska et al., 2024; Amoako et al., 2025). While most studies on STEs and their associated biogeochemical processes have focused on lower-latitude systems, our understanding of their occurrence and functioning in Arctic environments remains limited. However, recent research in Alaskan coastal lagoons by Demir et al. (2024) has confirmed that supra-permafrost groundwater flows, originating from the seasonally thawed active layer, can extend beyond coastal bluffs and beaches, even in areas underlain by permafrost. The presence of unfrozen, permeable coastal sediments thus creates pathways for fresh groundwater flow that mixes with recirculating seawater (as in STEs; Moore, 1999) and discharges into coastal zones, as observed in the Laptev Sea (Charkin et al., 2017) and in the Beaufort Sea along the Alaskan and Mackenzie coasts (Bullock et al., 2024; Kipp et al., 2025).

Absorbance- and fluorescence-derived indices are widely used to characterize the origin, reactivity, and transformation of aquatic DOM (Fichot & Benner, 2014; Meilleur et al., 2023; Stedmon et al., 2003). For instance, Fouché et al. (2020) identified permafrost-derived DOM as being predominantly low molecular weight (LMW), proteinaceous, and low in aromaticity, while DOM from the seasonally thawed active layer is characterized by high molecular weight (HMW), aromatic, and condensed organic compounds. However, this permafrost-derived signature appears to decline rapidly as DOM flows laterally downstream, suggesting a rapid turnover or transformation of permafrost DOM along the permafrost–fluvial continuum. The fate of these seasonally mobilized compounds at the land–ocean interface, particularly beyond beaches and coastal bluffs and along supra-permafrost flow paths, remains largely unknown in Arctic coastal environments. This study aims to characterize the transformation pathways of dissolved organic matter (DOM) released from the thawing of coastal Arctic bluffs and to highlight the role of beaches as active zones of transport and transformation of terrigenous DOM (tDOM). We hypothesize that DOM undergoes substantial compositional and optical changes along supra-permafrost flow paths, from the active layer to nearshore Arctic waters, driven by microbial degradation, photochemical processes, and organo-mineral interactions. Furthermore, we suggest that Arctic beaches act as both a sink and a biogeochemical reactor, modifying tDOM properties before their release into

111 the coastal ocean. To test these hypotheses, we implemented a fine-scale sampling strategy (<2 km) in the
112 Kugmallit Bay region (NWT, Canada) to monitor the optical characteristics and behavior of DOC and DOM
113 (including CDOM and FDOM) along the supra-permafrost flow, from coastal bluffs to the adjacent nearshore
114 waters. In parallel, we conducted targeted experiments to assess the affinity of permafrost-derived DOM and
115 DOC for amorphous Fe-hydroxides, aiming to clarify the role of Fe–organic interactions in DOM stabilization
116 and removal along supra-permafrost flow paths.

117

118 # 2 MATERIALS AND METHODS

119 ## *2.1 Site Description*

120 The study area is situated in the Inuvialuit Settlement Region of the Northwest Territories, near the Mackenzie
121 Delta, the fourth-largest river system discharging into the Arctic Ocean (Macdonald et al., 1998). The
122 Mackenzie River is a major source of freshwater, sediments, dissolved organic matter (DOM), and nutrients,
123 exerting a strong influence on the salinity and biogeochemistry of the Beaufort Sea (Holmes et al., 2012). The
124 tidal amplitude in Kugmallit Bay region is small (~0.3 m). Two field campaigns were conducted: the first from
125 July 24 to August 6, 2019, and the second from June 22 to August 31, 2021, coinciding with peak thaw
126 conditions. Approximately 60 samples were collected from four coastal sites characterized by continuous
127 permafrost and active thaw slumps, bordered by sandy and clay-rich beaches: Tuktoyaktuk Island, Peninsula
128 Point, Crumbling Point, and Reindeer Island (Fig. 1).

129 Tuktoyaktuk Island, the primary sampling site (N = 34; Fig. 2A), features a coastal bluff roughly 9 m high, 1.5
130 km long, and 100 m wide (Ouellette, 2021). Located southeast of Kugmallit Bay and opposite the Hamlet of
131 Tuktoyaktuk, the island is undergoing rapid coastal retreat, losing approximately 1.8 m of shoreline annually
132 due to storm events and permafrost thaw. This erosion rate has increased by 22% over the past 15 years (Berry
133 et al., 2021; Tanguy et al., 2023; Whalen et al., 2022), and the entire site is projected to vanish within the next
134 20–30 years (Jones et al., 2020). In front of the bluff lies a 50-m-wide beach composed of fine to medium sands

(0.3–0.5 m deep) overlying a frozen clay horizon (Fig. 2A). The exact submarine extension of this permafrost layer is unknown. Peninsula Point (N=7), southwest of Tuktoyaktuk Island within the Pingo Canadian Landmark, features a complex retrogressive thaw slump system underlain by a massive ice body ranging from 5 to 20 m in thickness (Mackay, 1986). Large, muddy lobes of thawed permafrost material and meltwater flow downslope toward the coast, intermittently covering the sandy intertidal zone (Fig. 2B). The shoreline has retreated at an average rate of ~3.4 m yr^{-1} between 1985 and 2018 (Hayes et al., 2022). Crumbling Point (N= 5), located at the northwest edge of Kugmallit Bay, is another retrogressive thaw slump system with similar geomorphological characteristics. Reindeer Island (N=11), north of Richards Island, is part of a lagoonal complex formed by thermokarst lakes and surrounded by coastal bluffs. Although specific erosion rates for this site are not yet available, they are likely comparable to regional averages for the Canadian Beaufort Sea (~0.5 m yr^{-1}; Solomon, 2005). However, localized retreat rates can be substantially higher as seen in nearby Pullen Island, where erosion exceeds 12 m yr^{-1} (Berry et al., 2021).

2.2 Water and Sediment Sampling

At each site, we carried out a localized sampling along a transect, from coastal thawed bluffs, through beaches and intertidal zones, to nearshore seawater as presented in Kipp et al. (2025). Meltwater and beach groundwater (here defined as porewater in sandy sediment) samples were collected from coastal permafrost slumps and the adjacent sandy shore, respectively, while seawater samples were collected 0.5 to 1 km offshore from each study site. Surficial sandy sediments from beaches in front of permafrost bluffs were also collected during the 2019 field campaign at Tuktoyaktuk Island (N = 3) and Peninsula Point (N = 2). Meltwater was sampled directly in puddles formed on the thaw slumps using a submersible pump. Beach groundwater was collected using push-point piezometers inserted ~50 cm depth into the sandy ground, above the frozen clay layer, within the intertidal zone, with continuous pumping via a Solinst® peristaltic pump. A massive ice sample was collected from a permafrost core collected at Richard Island, which was sectioned and thawed in a hermetically sealed, acid-cleaned bucket, before collecting the meltwater via a peristaltic pump. Finally, seawater samples were collected using a submersible pump placed 0.5 and 1 m below the surface from a small vessel in front of the slump systems. At each site, water samples were pumped into an online flow cell where salinity (S), temperature, pH

(at NBS scale), and oxygen saturation were monitored with a daily calibrated multiparametric probe (600QS, YSI Inc.). Note that these stations were likely under the influence of the Mackenzie River plume, which mainly controls the water chemistry and optical signature in the region (see Lizotte et al., 2022, and references therein).

Water samples were collected for CDOM/FDOM into acid-washed 60 mL glass amber bottles after on-line filtration through a 0.22 µm Millipore Opticap® XL4 cartridge with a Durapore® membrane. The samples were stored in the dark at 4 °C. Total dissolved Fe (Fetot) samples were collected in 60 mL metal-free Falcon® tubes after filtration through the same 0.22 µm Millipore Opticap cartridge. The samples were acidified with 3 drops of 70 % nitric acid to prevent the re-oxidation of reduced trace metals and stored at 4 °C. DOC samples were taken using 60 mL acid-cleaned polypropylene syringes and rapidly filtered with pre-combusted (450 °C for 5–6 hours) 25mm Whatman GF/F (0.7 µm) and stored in pre-combusted and acid-washed 12 mL borosilicate EPA tubes with PTFE caps. The same day, the DOC samples were acidified to pH <2 with high-purity HCl 2N and stored in the dark at 4 °C until analysis. During the 2019 campaign, samples were also collected in 30 ml scintillation vials, hermetically sealed for further water stable isotope analysis.

2.3 Chemical and Optical Analysis

Total organic carbon (TOC) content was measured on freeze-dried, ground and homogenized sediment using a CHNSO analyzer (Costech ECS 4010 CHNSO analyzer®; accuracy < 0.3%). Reactive Fe-hydroxide content was determined on the same sediment samples, extracted using the citrate-dithionite-bicarbonate (CDB) reduction method of Mehra and Jackson (1960), as modified by Lalonde et al. (2012), and previously applied to sandy sediments by Sirois et al. (2018). Briefly, reactive Fe-hydroxides are reductively dissolved with dithionite at circumneutral pH (bicarbonate buffer) using citrate as a complexing agent to keep dissolved Fe in solution. Fe in solution was analyzed using a Microwave Plasma Atomic Emission Spectrophotometer (4200 MP-AES; Agilent Technologies). The detection limit of the method is 2.4 µg L^{-1} for Fe concentration at a wavelength of 391 nm and analytical uncertainties were <5%.

Stable isotopes of water were analyzed by EA-IRMS during the following year after the collection. Accuracies are ±0.05 ‰ and ±1 ‰ for $\delta^{18}O$ and $\delta^{2}H$, respectively. Reference materials were used throughout the isotopic

water analyses and isotopic analyses are reported compared to the international Vienna Standard Mean Ocean Water (VSMOW). DOC samples were analyzed a few weeks after data collection by Total Organic Carbon analyzer (TOC-VCPN Shimadzu) based on the method of Wurl and Tsai (2009). The analytical uncertainty was less than 4 %, while the detection limit was 5.8 µmol L^{-1}. To ensure instrument stability, fresh acidified deionized water (blank) and a standard solution were regularly analyzed. The concentration of total dissolved iron (Fe_{tot}) was measured according to the ferrozine method proposed by Stookey (1970) and adapted by Viollier et al. (2000). The detection limit of the method was 0.4 µmol L^{-1} and the reproducibility was better than 0.3 %.

Absorbance and fluorescence spectroscopy were used for the measurement of the chromophoric and fluorescent fractions of DOM (CDOM and FDOM) a few weeks after sampling. The CDOM absorbance was measured using a Lambda 850 UV-VIS Perkin Elmer spectrophotometer with 1 cm path-length quartz cuvettes. Measurements were taken from 220 to 800 nm at 1 nm intervals with a scanning speed of 100 nm min^{-1} and a 5 nm slit width. Blanks and references were measured using fresh Milli-Q water. The FDOM was measured concomitantly using a Varian Cary Eclipse spectrofluorometer. Fluorescence spectra were measured within the emission wavelengths of 220 to 600 nm and the excitation wavelengths of 220 to 450 nm at 5 nm intervals as described by Couturier et al. (2016). Similarly, fresh Milli-Q water was used as a blank to rinse the cuvette in between samples. Fresh deionized water was used as a blank and absorbance measurements were used to correct the inner-filter effect and the dataset was corrected for Rayleigh and Raman scattering, according to the method used by Pucher et al. (2019).

2.4 Optical-derived indices and PARAFAC model

Absorbance and fluorescence indices were extracted using the staRdom toolbox on the R Studio Software (Pucher et al. 2019). Different indices were explored, including aCDOM350, BIX, HIX, FI, SUVA254 and SR. However, only three were reported here to characterize the DOM pool, as they showed distinct variations among the different categories of samples (e.i. beach groundwater, meltwater, massive ice, and seawater). The spectral absorption coefficient at 350 nm (aCDOM350) was used as a tracer of CDOM absorption and content. It was calculated as 2.303 times the absorbance at the wavelength λ=350 nm divided by the path length of the cuvette

211 (m). The specific UV absorbance (SUVA254 in mgC L^{-1}) was calculated as the absorbance at the wavelength
212 λ=254 nm divided by the DOC concentration. It allows tracking the CDOM aromaticity (Weishaar et al. 2003):
213 greater SUVA254 values correspond to a greater degree of aromaticity (Helms et al. 2008). It has also been
214 shown as positively correlated with the molecular weight of the DOM compounds. In the FDOM pool, the
215 humification index (HIX) corresponds to the peak area under emission of 435–480 nm divided by the peak area
216 under emission of 300–345 nm, at an excitation of 254 nm. HIX is an indicator of humic substances and the
217 extent of humification of DOM compounds (Hansen et al., 2016; Ohno, 2002): higher HIX indicates a greater
218 humification of the DOM source and HMW compounds.

219 In combination with the absorbance and fluorescence indices, a PARAFAC model – based on over 250 Arctic
220 and subarctic coastal water samples – was developed to investigate further the composition and the sources of
221 FDOM across samples (Bro 1997; Murphy et al. 2013; Stedmon et al. 2003). Three components were validated
222 using the method adapted from Pucher et al. (2019), in R studio (R^2>92 %). The components were also matched
223 with the literature for identification and external validation, using OpenFluor (Murphy et al. 2013). The three
224 fluorescing peaks (C1-3) identified are presented in Fig. 3, and their theoretical characteristics based on the
225 literature are summarized in Table 1. Briefly, C1 and C3 components are mainly related to terrestrial and humic-
226 like compounds of high (HMW) and low molecular weight (LWM), respectively. In contrast, the C2 component
227 is likely related to freshly produced protein-like compounds of autochthonous origin and is mainly composed
228 of LMW compounds.

229 ***2.5 Affinity of permafrost derived DOM with Fe-hydroxides***

230 Iron-spiked experiments were performed to assess the affinity of flowing DOM and DOC with amorphous
231 reactive Fe-hydroxides. Samples of beach groundwater, seawater and meltwater were collected in 1-L acid-
232 washed glass bottles. In the laboratory, ~20 mM of $FeCl_2 \cdot 4H_2O$ were added to filtered (Pall® GWV High-
233 Capacity Groundwater Sampling Capsule, 0.45 µm porosity) water samples. The concentration of Fe was
234 intentionally added in excess compared to Fe_{tot} concentration measured in the samples (median Fe_{tot}
235 concentration ~ 1.1 µmol L^{-1}; with maximum values of 820 µmol L^{-1} in beach groundwater) to favor the

oxidative precipitation of amorphous Fe-hydroxides. The experiments were performed rapidly after the sampling (<24h) during the 2021 campaign. The experimental bottles were kept in the dark, at room temperature (~ 21°C). They were continuously air-bubbled to maintain well-oxygenated conditions and favoured the precipitation of Fe-hydroxides. Sub-samples for DOC and CDOM analysis were collected at times 0, 6, 12, 24 and 48 hours. DOC and CDOM samples were analyzed as previously described.

3 RESULTS AND DISCUSSION

3.1 Physico-chemical characteristics along the permafrost-nearshore continuum

In this study, we refer to samples collected at the nearshore as "seawater"; nevertheless, we acknowledge that these samples more accurately represent a brackish environment, with salinity S values ranging from 0.5 to 20, mostly related to the Mackenzie River plume occurrence. The massive ice and meltwater samples exhibited the lowest salinities with S<1, whereas the salinity of beach groundwater samples ranged between 0.2 and 5.4. The S range measured in beach groundwater samples mostly reflected the tidal and wave pumping effect and the recirculation of the infiltrated seawater within the permeable sediments (Santos et al., 2012). The higher salinities (5.4<S<20.0) were only measured in seawater samples. The temperature varied between 8.1 and 16.7 °C (with a mean value of 13.0 ± 2.6 °C), with the higher temperatures measured in meltwater and some beach groundwater samples. Oxygen saturations ranged from 6 to 141 % of saturation. The nearshore surface seawater and the meltwater samples were all oversaturated due to mixing and photosynthetic processes. However, the low-salinity beach groundwater samples exhibited low oxygen saturation (6 - 48 %) despite the recirculation of well-oxygenated seawater. Redox oscillations and transitory oxygen-depleted conditions are observed in micro- and meso-tidal sandy intertidal zones (Hébert et al. 2022; Sirois et al. 2018; Waska et al. 2021), where oxygen input from tidal processes is rapidly consumed by heterotrophic processes (Chaillou et al., 2018, 2024; Moore et al., 2024). Regarding pH (NBS scale), the highest median values were observed in both meltwater and seawater (7.9), while beach groundwater exhibited a slightly lower median pH of 7.5, ranging from 7.0 to 8.0. Although pH data for massive ice samples were not available, their values likely fall within the lowest range of

measured pH. This assumption is based on the origin of the massive ice in the region, which is thought to result from intrasedimental processes (e.g., ice intrusion and segregation) rather than from relict glacial ice (Mackay and Dallimore, 1992).

3.2 Origin of the subsurface water flow in the intertidal zone

Little is known about the hydro(geo)logical connectivity between supra-permafrost groundwater and Arctic coastal seawater (Letcher et al., 2017). However, recent studies and conceptual models, mostly developed for lower-latitude regions, suggest that key transport mechanisms of water and permafrost-derived solutes to the coastal zone are likely governed by three main pathways (Walvoord & Kurylyk, 2016): (i) riverine transport, which includes both active layer runoff and contributions from deeper groundwater (Dittmar & Kattner, 2003; Demir et al., 2024); (ii) coastal erosion, which directly delivers organic-rich permafrost soils and particulate matter into the marine environment (Kipp et al., 2018); and (iii) submarine groundwater discharge (SGD) through subterranean estuaries (STEs), where supra-permafrost groundwater mixes with recirculating seawater before entering nearshore waters (Demir et al., 2024; Kipp et al., 2025). The $\delta^{18}O$ and $\delta^{2}H$ results support the theoretical model in which beach groundwater represents a mixture of supra-permafrost groundwater flowing seaward and recirculating seawater advected landward (Fig. 2). The $\delta^{18}O$ and $\delta^{2}H$ values measured in water samples collected in 2019, mostly at Tuktoyaktuk Island, Peninsula Point sites, and Crumbling Point (Fig. 1), ranged from -28 to -10 ‰ and from -215 to -82 ‰, respectively, the massive ice sample (N=1) presents the most depleted signature (Fig. 4). These depleted values are largely explained by low air temperatures and are typical of permafrost hydrology reported in the western Arctic (Fritz et al. 2011; Utting et al., 2012). The samples are well aligned along the local meteoric water line (LMWL; $\delta^{2}H = 7.39 \times \delta^{18}O - 6.70$; Fritz et al., 2022), regardless of their salinity values, except for the three (3) meltwater samples that are slightly below it, likely due to evaporation processes at the surface. The alignment of the different samples along the LMWL regression line suggests a common meteoric origin, probably from the permafrost watershed. The supra-permafrost groundwater flow that transits through the beach sediment does not seem to be affected by surficial processes (e.g. evaporation process), as observed in a few meltwater samples, likely limiting photochemical degradation of the flowing DOM. However, the high range of isotopic values, from -25 to -12 ‰ and -192 to

-112‰ for $\delta^{18}O$ and $\delta^{2}H$, respectively, suggested a mixing between depleted thawed waters (as surficial meltwater and supra-permafrost groundwater) and enriched seawater, as expected in a STE system. These results are consistent with the recent study by Kipp et al. (2025), which reported elevated activities of radon isotopes (^{222}Rn) in the same beach groundwater samples. Radon, a noble gas, escapes rapidly upon exposure to the atmosphere, indicating a groundwater origin and minimal atmospheric interaction. These authors proposed that thaw water derived from massive ground ice is transported into the supra-permafrost groundwater system, where it becomes diluted by recirculating seawater (e.g. offshore water from the Mackenzie River) percolating through the beach sediments. Our findings support the presence of this dynamic mixing zone within sandy beach sediments, where stable isotopes, salinity, oxygen saturation, and pH fluctuate due to the infiltration of offshore seawater.

The absence of light and the combined fluctuations in pH, salinity, and redox conditions in beach groundwater samples were conducive for a complex network of redox reactions, including the remineralization of organic matter and the cycling of iron between its oxidized (Fe(III, IV)) and reduced (Fe(II)) states.

3.3 Behaviour of the DOC and DOM pool

The DOC concentrations dropped from 2,360 µmol L^{-1} in meltwater samples to 236 µmol L^{-1} in the saltiest seawater sample (S=20.0; Fig. 5A). The concentrations declined sharply along the supra-permafrost flow path to reach values below 400 µmol L^{-1} in beach groundwater samples. DOC concentrations in seawater samples, and, to a lesser extent, in beach groundwater, closely followed the theoretical mixing line connecting the freshest and saltiest endmembers. This pattern suggests that dilution becomes the dominant process controlling DOC behaviour once supra-permafrost flow enters the STE and is exported to adjacent coastal seawaters. Absorption coefficients at 350 nm (aCDOM350) ranged from 2 to a maximum of 134 m^{-1}, the latter observed in a meltwater sample (Fig. 5B). Like DOC concentrations, the aCDOM350 values declined sharply along the flow path, with a median value of 24.0 m^{-1} in meltwater samples and median values of 8.4 and 7.8 m^{-1} in beach groundwater and seawater, respectively. However, unlike DOC, aCDOM350 values in beach groundwaters and seawater did not follow a simple dilution trend between the freshest and saltiest endmembers. The HIX indices showed a

311 wide range of values across all sample types. Median values tended to decrease along the continuum, from 3.5
312 (unitless) in meltwater samples to 1.4 in beach groundwater, and 0.8 in seawater (Fig. 5C). Similar to
313 aCDOM350, HIX values in beach groundwater and seawater did not follow a dilution pattern along the salinity
314 gradient. Whereas DOC, aCDOM350, and HIX values declined along the flow path, SUVA254 indices showed
315 an increasing trend from the massive ice and meltwater samples toward beach groundwater and adjacent
316 nearshore seawater. The median SUVA254 value rose from 2.4 mg C L^{-1} in the meltwater to 2.9 mg C L^{-1} in
317 beach groundwater, and further reached to 3.4 mg C L^{-1} in seawater samples (Fig. 5D). With a few exceptions,
318 SUVA254 values in beach groundwater and seawater closely followed the theoretical dilution line along the
319 salinity gradient.

320 DOC concentration and aCDOM are commonly used as proxies to assess both the quantity and optical
321 properties of the DOM pool in aquatic systems. The relationship between these two parameters provides insights
322 into the biogeochemical sources and transformation processes shaping DOM composition along environmental
323 gradients (Massicotte et al., 2017; Fichot and Benner, 2011; Spencer et al., 2013; Stedmon et al., 2003). A
324 strong correlation between DOC and aCDOM typically indicates that CDOM represents a stable and consistent
325 fraction of the total DOM pool, a linear relation frequently observed in freshwater systems, where DOC and
326 aCDOM are tightly coupled (Frenette et al., 2012; Massicotte et al., 2017 and references therein). However,
327 deviations from this relationship, referred to as DOC-CDOM decoupling, suggest shifts in DOM composition
328 and point to selective processing of specific DOM fractions. While mixing (or dilution) and microbial
329 degradation affect both DOM and DOC with similar rates, processes such as photo-oxidation and organo-
330 mineral interactions can selectively modify optically active and non-optically active components of DOM.
331 These mechanisms lead to shifts in DOM composition along the land-ocean continuum (Del Vecchio & Blough,
332 2004; Nelson et al., 1998; Nelson & Siegel, 2013). For example, Couturier et al. (2016) reported a decoupling
333 between CDOM-DOC in a subarctic STE, where high molecular weight (HMW) DOM compounds were largely
334 retained, limiting their export to nearshore adjacent seawater. In such environments, the so-called “iron curtain”
335 (e.g. a zone of intense Fe cycling at the oxic-anoxic interface) acts as a geochemical barrier, promoting the
336 sequestration of tDOM (Sirois et al., 2018). Although the exact mechanisms of Fe-DOM interactions in such

shallow STEs remain incompletely understood (adsorption vs. co-precipitation), Linkhorst et al. (2017) demonstrated that amorphous Fe-hydroxides preferentially trap HMW DOM enriched in aromatic, carboxylic, and hydroxyl functional groups, such as altered lignin and polysaccharide compounds of terrestrial origin, over more aliphatic-rich compounds characteristic of marine DOM. As in soils and cohesive marine sediments, molecular fractionation of DOM within STEs tends to promote the *in situ* degradation and/or preferential export of non-Fe-stabilized, marine-derived DOM to coastal waters (Linkhorst et al., 2017; Sirois et al., 2018; Waska et al., 2022; Zhou et al., 2023).

The strong decoupling between DOC and aCDOM350, particularly in meltwater, massive ice, and beach groundwater samples (Fig. 6), indicates that DOC and aCDOM follow different trajectories (Fig. 5A and 5B) and are subject to selective transformation processes. Given the light-limited conditions in beach groundwater environments, microbial degradation and mineral–organic interactions are likely the dominant factors controlling the fate and composition of the DOM pool. Acting concurrently, these processes contribute to the reduction of both DOC and CDOM concentrations along the supra-permafrost flow path and drive compositional changes in DOM, notably a decrease in humification and a shift toward lower molecular weight material as revealed by HIX indices (Fig. 5A to 5C). Despite this general decline in the DOM pool, the impact on DOM aromaticity (as indicated by SUVA254) remains relatively weak. SUVA254 values tend to increase slightly along the flow path, likely reflecting the dilution effect with the offshore seawater (Fig. 5D). The low fluorescent and biological indexes (FI<1.5, 0.5<BIX<0.9; data not shown) together with elevated SUVA254 values of seawater samples, suggest that the "marine"-derived DOM is more decomposed and refractory, likely influenced by extensive terrestrial input and degradation during the transport in the Mackenzie River watershed and plume (McKnight et al. 2001; Huguet et al. 2009).

3.4 The decoupling between DOC and DOM and the organo-mineral interactions

The *in situ* production of a new DOM pool, characterized by more degraded components with lower molecular weights and higher aromaticity, along the supra-permafrost flow path cannot be ruled out despite the low TOC content in the surficial sandy sediment (TOC< 0.50% dry sediment; Table 2). Similar patterns have been

observed in transgressive subarctic STEs (Hebert et al., 2022) and in areas with buried peat lenses (Waska et al., 2021), where ancient sedimentary organic matter preserved in paleosols acts as a hotspot for terrestrial DOM production along the groundwater flow path. Such inputs can significantly influence the chemical and optical properties of coastal waters. Moreover, the presence of permafrost extending below the STE suggests that additional particulate organic matter reservoirs may be mobilized under thawing conditions, further contributing to DOM production, transformation and export. These deeper *in situ* inputs may explain the very depleted stable water isotopic signature of a few beach groundwater samples and the high radon activities reported by Link et al. (2025). Further efforts are needed to improve our understanding of Arctic beach hydrogeology by using geochemical and molecular proxies.

Despite their low total organic carbon (TOC) content, sandy sediments can act as hotspots of redox activity (Anschutz et al., 2009). Elevated DOC and DOM concentrations, combined with fluctuating oxygen levels and salinity gradients, promote the reductive dissolution and oxidative precipitation of redox-sensitive elements at oxic–anoxic interfaces, as well as coagulation processes. The presence of reactive Fe-hydroxide coatings on sandy sediment surfaces, along with intermittently high total dissolved iron (median Fe_{tot} reaching 820 µmol L^{-1}; Fig. 7A) concentrations in beach groundwater, suggests the formation of Fe-OM associations. The extent of Fe–OM coprecipitation or coagulation is governed by several factors, including the Fe : DOC molar ratio, organic matter composition, Fe speciation, and physicochemical parameters such as pH and salinity. As previously explained, the chemical nature of DOM plays a critical role in its interaction with mineral surfaces: higher molecular weight, aromatic, oxygen-rich terrigenous DOM tends to bind more strongly to Fe(III) than aliphatic, marine-derived DOM (Linkhorst et al., 2017). Additionally, slightly acidic conditions promote Fe(III)–DOM coagulation (Nierop et al., 2002; Amoako et al., 2025). In beach groundwater, pH values were consistently lower than those in seawater (ranging from 7.0 to 8.0 versus ~8.2 in seawater), likely reflecting proton production associated with mineralization processes. This interpretation is supported by elevated dissolved inorganic carbon (DIC) concentrations in several 2019 samples, which exceeded 3,000 µmol L^{-1} (Lizotte et al., 2022). Furthermore, the high Fe : DOC ratio observed in beach groundwater (~0.00237; Fig. 7B) indicates strong interactions between dissolved iron and organic carbon in these environments.

388 The Fe-spiking experiments conducted on seawater, groundwater, and meltwater samples revealed two distinct
389 patterns for DOC and CDOM dynamics. Although the experimental design did not allow us to assess long-term
390 changes in CDOM optical properties, the results demonstrate a strong affinity between DOM and freshly
391 precipitated reactive Fe-hydroxides. Immediately following Fe addition, DOC concentrations dropped sharply,
392 with an initial loss of approximately 40% across all sample types. This was followed by a slower decline over
393 the subsequent hours, reaching minimum concentrations at around 6 hours post-addition (Fig. 8A). However,
394 after 48 hours, partial DOC desorption from Fe-mineral phases was observed. Since the experiment lasted only
395 48 hours, it remains uncertain whether DOC concentrations would have continued to rise or eventually
396 plateaued. Nevertheless, the net DOC loss in solution over the experiment was moderate (32%, 34%, and 30%
397 for seawater, beach groundwater, and meltwater, respectively), suggesting reversible interactions between Fe-
398 hydroxides and DOC. Importantly, the similar DOC removal and recovery patterns across all salinity regimes
399 indicate that the Fe–DOC complexation process is relatively insensitive to salinity under the tested conditions.
400 In contrast to DOC, the loss of aCDOM350, used here as a proxy for terrestrial DOM (tDOM), was nearly
401 complete within 6 hours following the Fe addition, with concentrations remaining consistently low for the
402 remainder of the experiment (Fig. 8B). By the end of the 48-hour incubation, net tDOM removal from solution
403 reached 62%, 57%, and 94% of the initial concentrations in seawater, beach groundwater, and meltwater
404 samples, respectively. The particularly high tDOM loss observed in the meltwater samples is consistent with
405 the presence of high molecular weight (HMW) compounds with a high degree of humification, compounds
406 known to be especially prone to complexation and stabilization by amorphous Fe phases.

407 To further clarify these interactions, the CDOM/DOC ratios observed across different sample types support the
408 hypothesis that Fe-hydroxides selectively interact with specific fractions of the DOM pool. In seawater, the
409 CDOM/DOC ratio decreased markedly following Fe addition, suggesting that a substantial portion of the
410 optically active DOM had a strong affinity for freshly precipitated Fe-hydroxides, resulting in rapid removal
411 from solution. In contrast, meltwater and beach groundwater samples exhibited relatively stable CDOM/DOC
412 ratios throughout the experiment. This stability suggests either a reduced reactivity of their DOM with Fe-
413 hydroxides or that Fe-reactive DOM fractions had already been removed from solution, likely due to prior

interactions and stabilization within the sediment matrix. The exact mechanism controlling the molecular fractionation of the DOM pool in supra-permafrost groundwater remains to be determined, and further studies are required to explore the role of the organic-mineral interaction to better quantify the export of thaw material.

3.5 PARAFAC components in the DOM pool

Among the three fluorescent components identified by the PARAFAC model, the protein-like component C2 dominated the FDOM pool across all sample types and salinities (Table 1; Fig. 9). No clear trend in the distribution of components was observed along the salinity gradient. However, C2 exhibited a strong negative correlation with both humic-like components (C1 and C3) and the humification index (HIX), with correlation coefficients of $r^2 = –0.89$ ($p < 0.001$) for C1/C3 and $r^2 = –0.92$ ($p < 0.001$) for HIX. The median values of C2 increased progressively along the continuum, peaking in the seawater samples. In contrast, the humic-like components C1 and C3 were positively correlated with each other ($r^2 = 0.81$, $p < 0.001$) and with HIX ($r^2 = 0.85$ and 0.69, respectively; $p < 0.001$). Similar to the patterns observed for HIX, DOC, and aCDOM350, both C1 and C3 declined along the flow path, with the lowest median values found in seawater.

Massive ice and meltwater samples were predominantly composed of humic-like, high molecular weight (HMW), and terrestrially derived FDOM (component C1), and were rich in both tDOM and DOC. This composition is consistent with active layer-derived FDOM described by Fouché et al. (2020), who emphasized the key role of the active layer in seasonally mobilizing humic-like material. Our findings support this, suggesting that meltwater and massive ice act as important precursors of supra-permafrost solutes flowing to the coastal ocean through Arctic beaches. As DOM is transported along the flow path, a marked loss of humic-like compounds is observed, coinciding with an increase in biologically derived, tyrosine-like FDOM (component C2), typically associated with microbial production (Table 1 and references therein). This shift mirrors transformations reported by Fouché et al. (2020), where microbial processing converts DOM into lower molecular weight, protein-like material. In this context, the presence of non-Fe-stabilized DOM and redox-active conditions likely favour microbial mineralization, contributing to the formation of low molecular weight (LMW) and protein-like compounds.

4 CONCLUSION

This study reveals rapid declines in DOC and CDOM concentrations along the diffuse and non-point source supra-permafrost groundwater flow from coastal permafrost bluffs through sandy beach sediments and to adjacent nearshore seawater. The findings highlight the importance of microbial degradation and mineral-organic interactions, particularly with Fe-hydroxides, in transforming and retaining permafrost-derived DOM. These processes occur primarily within Subterranean Estuaries (STEs), where they selectively remove humic-like, high molecular weight DOM and alter its composition before it reaches the Arctic Coastal Ocean. Our findings suggest that intertidal and nearshore zones, including STEs, may act as a transient or permanent carbon sink, modulating or limiting the export of terrestrial carbon and enhancing CO_2 release through microbial mineralization. Given accelerating permafrost thaw and coastal erosion, understanding these nearshore processes is critical for constraining Arctic carbon budgets and predicting their role in global climate feedbacks.

Data availability: Along with this submission, the dataset used in this research was submitted and accepted for publication to Pangaea Data Publisher (www.pangaea.de). Once this article accepted for publication, the moratorium in place will be lifted and the dataset generated during the study will be freely available in the Pangaea repository. Here is the hyperlink and DOI toward the dataset: https://doi.pangaea.de/10.1594/PANGAEA.960986

Author contribution: Aude Flamand: Investigation, Conceptualization, Methodology, Formal analysis, Validation, Data curation, Visualization, Writing - Original Draft Preparation, Writing - Review & Editing; Jean-François Lapierre: Supervision, Methodology, Validation, Data curation, Writing - Review & Editing; Gwénaëlle Chaillou: Conceptualization, Methodology, Validation, Data curation, Supervision, Project administration, Funding acquisition, Writing - Review & Editing.

Competing interests: The authors declare that there are no competing interests.

Acknowledgements: This project was made possible through the tremendous support of the hunters and trappers committee, the hamlet and town council, in addition to several members of the Inuvialuit Nunangit Sannaiqtuaq community of Tuktoyaktuk. The authors would like to express their gratitude to Dustin Whalen (NRCan) for his invaluable contributions that made the fieldwork possible, as well as for his assistance in providing resources and coordinating the fieldwork. We also want to thank Charlotte Irish, James Pokiak, Angus Robertson, Bay Berry, and Brian Mayhew for their precious help during fieldwork in the summers of 2019 and 2021. We thank Claude Belzile for analyzing the DOC sample at ISMER-UQAR, Frédérik Bélanger for conducting the CDOM and FDOM analysis of the 2019 samples and Antoine Biehler for his help with database management. We also want to thank Simon Bélanger (UQAR) and Celine Guéguen (U. Sherbrooke) for providing early feedback on this manuscript. This work represents a contribution to the scientific programs of Nunataryuk, ArcticNet, and Québec-Océan.

Financial support: Financial support for this project has been provided by the Network of Centers of Excellence of Canada ArcticNet (grant no. P-66), by Québec-Océan, funded through the Fonds de Recherche du Québec – Nature et Technologies, and by the Aurora Research Institute – Aurora College. The authors received additional funding from NSERC (RGPIN-2021-04332 to GC) and in-kind support from Natural Resources Canada (Climate Change Geoscience Program and Polar Continental Shelf Program; grant no. 007-19) for logistics support (equipment and helicopter time), and Crown–Indigenous Relations and Northern Affairs Canada (Climate Change Preparedness in the North program, CCPN grant no. CCPN PN-NT-077-2018; Beaufort Sea Regional Strategic Environmental Assessment Program, BRSEA agreement no. 239) in the form of consultation tour of the ISR (March 2019). AF also received grants from the Northern Scientific Training Program (NSTP) and from Québec-Océan.

5 REFERENCES

Amoako, K., Reckhardt, A., Roberts, M., Meyer, R., Brick, S., Dittmar, T., and Waska, H.: Organo-mineral interactions modulateorganic carbon retention and mobility in adeep subterranean estuary of a high-energybeach. Frontiers in Water 7:1507564. 2025

Anschutz, P., T. Smith, A. Mouret, J. Deborde, S. Bujan, D. Poirier, and P. Lecroart: Tidal sands as biogeochemical reactors. Estuarine, Coastal and Shelf Science 84 (1): 84–90. https://doi.org/10.1016/j.ecss.2009.06.015, 2009.

Benner, R., and Amon, R. M.: The size-reactivity continuum of major bioelements in the ocean, Annu. Rev. Mar. Sci., 7, 185–205, https://doi.org/10.1146/annurev-marine-010213-135126, 2015.

Berry, H. B., Whalen, D., and Lim, M.: Long-term ice-rich permafrost coast sensitivity to air temperatures and storm influence: lessons from Pullen Island, Northwest Territories, Canada, Arct. Sci., 7, 723–745, https://doi.org/10.1139/as-2020-0003, 2021.

Bristol, E. M., Connolly, C. T., Lorenson, T. D., Richmond, B. M., Ilgen, A. G., Choens, R. C., Bull, D. L., Kanevskiy, M., Iwahana, G., and Jones, B. M.: Geochemistry of coastal permafrost and erosion-driven organic matter fluxes to the Beaufort Sea near Drew Point, Alaska, Front. Earth Sci., 8, https://doi.org/10.3389/FEART.2020.598933, 2021.

Bro, R.: PARAFAC. Tutorial and applications, Chemometr. Intell. Lab., 38, 149–171, https://doi.org/10.1016/S0169-7439(97)00032-4, 1997.

Bullock, E. J., Schaal, I. V., Cardenas, M. B., McClelland, J. W., Henderson, P. B., & Charette, M. A. : Seasonality of submarine groundwater discharge to an Arctic coastal lagoon. Limnology and Oceanography. https://doi.org/10.1002/lno.12585, 2024.

Chaillou, G., Lemay-Borduas, F., Larocque, M., Couturier, M., Biehler, A., and Tommi-Morin, G.: Flow and discharge of groundwater from a snowmelt-affected sandy beach, J. Hydrol., 557, 4–15, https://doi.org/10.1016/J.JHYDROL.2017.12.010, 2018.

Chaillou, G., Tommi-Morin, G., and Mucci, A. : Production and fluxes of inorganic carbon and alkalinity in a subarctic subterranean estuary. Front. Mar. Sci. 11:1323463. https://doi.org/10.3389/fmars.2024.1323463, 2024.

Charkin, A. N., Van Der Loeff, M. R., Shakhova, N. E., Gustafsson, Ö., Dudarev, O. V., Cherepnev, M. S., et al.: Discovery and characterization of submarine groundwater discharge in the Siberian Arctic seas: A case study in the Buor-Khaya Gulf, Laptev Sea. The Cryosphere, 11, 2305–2327. https://doi.org/10.5194/tc-11-2305-2017, 2017.

Charette, M. A., and Sholkovitz, E. R.: Oxidative precipitation of groundwater-derived ferrous iron in the subterranean estuary of a coastal bay, Geophys. Res. Lett., 29, 85-81, https://doi.org/10.1029/2001GL014512, 2002.

Charrette, M. A., and Sholkovitz, E. R.: Trace element cycling in a subterranean estuary: Part 2. Geochemistry of the pore water, Geochim. Cosmochim. Ac., 70, 811–826, https://doi.org/10.1016/j.gca.2005.10.019, 2006.

Chen, C. M., Dynes, J. J., Wang, J., Sparks, D. L. : Properties of Fe-Organic Matter Associations via Coprecipitation versus Adsorption. Nature Reviews Earth & Environment 48 (23), 13751– 13759, https://doi.org/10.1021/es503669u, 2014.

522 Couturier, M., Nozais, C., and Chaillou, G.: Microtidal subterranean estuaries as a source of fresh terrestrial
523 dissolved organic matter to the coastal ocean, Mar. Chem., 186, 46–57,
524 https://doi.org/10.1016/j.marchem.2016.08.001, 2016.

525 Del Vecchio, R., and Blough, N. V.: Spatial and seasonal distribution of chromophoric dissolved organic
526 matter and dissolved organic carbon in the Middle Atlantic Bight, Mar. Chem., 89, 169–187,
527 https://doi.org/10.1016/j.marchem.2004.02.027, 2004.

528 Demir, C., McClelland, J. W., Bristol, E., Charette, M. A. & Cardenas, M. B.: Coastal Supra-Permafrost
529 Aquifers of the Arctic and Their Significant Groundwater, Carbon, and Nitrogen Fluxes. Geophysical Research
530 Letter 51, e2024GL109142, 2024.

531 Frenette, J-J., Massicotte, P., and Lapierre, J-F.: Colorful Niches of Phytoplankton Shaped by the Spatial
532 Connectivity in a Large River Ecosystem: A Riverscape Perspective. PLoS ONE, 7(4), e35891,
533 https://doi.org/10.1371/journal.pone.0035891, 2012.

534 Fichot, C. G., and Benner, R.: A novel method to estimate DOC concentrations from CDOM absorption
535 coefficients in coastal waters, Geophys. Res. Lett., 38, https://doi.org/10.1029/2010GL046152, 2011.

536 Fichot, C. G., Kaiser, K., Hooker, S. B., Amon, R. M. W., Babin, M., Bélanger, S., Walker, S. A., and
537 Benner, R.: Pan-Arctic distributions of continental runoff in the Arctic Ocean, Sci. Rep.-UK, 3, 1053,
538 https://doi.org/10.1038/srep01053, 2013.

539 Fichot, C. G., Kaiser, K., Hooker, S. B., Amon, R. M. W., Babin, M., Bélanger, S., Walker, S. A., and Benner,
540 R.: Pan-Arctic distributions of continental runoff in the Arctic Ocean, Scientific Reports 3, 1053. https://doi.org/
541 10.1038/srep01053, 2013.

542 Fichot, C. G., and Benner, R.: The fate of terrigenous dissolved organic carbon in a river-influenced ocean
543 margin, Global Biogeochem. Cy., 28, 300–318, https://doi.org/10.1002/2013GB004670, 2014.

544 Fouché, J., Christiansen, C. T., Lafrenière, M. J., Grogan, P., and Lamoureux, S. F.: Canadian permafrost stores
545 large pools of ammonium and optically distinct dissolved organic matter, Nat. Commun., 11, 4500,
546 https://doi.org/10.1038/s41467-020-18331-w, 2020.

547 Fritz, M., Wetterich, S., Meyer, H., Schirrmeister, L., Lantuit, H., and Pollard, W. H.: Origin and characteristics
548 of massive ground ice on Herschel Island (western Canadian Arctic) as revealed by stable water isotope and
549 hydrochemical signatures, Permafrost Periglac., 22, 26–38, https://doi.org/10.1002/ppp.714, 2011.

550 Fritz, M., Vonk, J. E., and Lantuit, H.: Collapsing Arctic coastlines, Nat. Clim. Change, 7, 6–7,
551 https://doi.org/10.1038/nclimate3188, 2017.

552 Fritz, M., Wetterich, S., McAlister, J., and Meyer, H.: A new local meteoric water line for Inuvik (NT, Canada),
553 Earth Syst. Sci. Data, 14, 57–63, https://doi.org/10.5194/essd-14-57-2022, 2022.

554 Guo, L., Ping, C. L., and Macdonald, R. W.: Mobilization pathways of organic carbon from permafrost to
555 arctic rivers in a changing climate, Geophys. Res. Lett., 34, https://doi.org/10.1029/2007GL030689, 2007.

556 Hansen, A.M., Kraus, T.E.C., Pellerin, B.A., Fleck, J.A., Downing, B.D. and Bergamaschi, B.A.: Optical
557 properties of dissolved organic matter (DOM): Effects of biological and photolytic degradation. Limnol.
558 Oceanogr., 61: 1015-1032. https://doi.org/10.1002/lno.10270, 2016.

559 Hayes, S., Lim, M., Whalen, D., Mann, P. J., Fraser, P., Penlington, R., and Martin, J.: The role of massive ice
560 and exposed headwall properties on retrogressive thaw slump activity. J. Geophys. Res. Earth Surf., 127,
561 e2022JF006602. https://doi.org/10.1029/2022JF006602, 2022.

562 Hayes, S.: Massive ice and topographic controls on retrogressive thaw slump dynamics: Peninsula point,
563 western canadian arctic (Order No. 28187262). Doctoral thesis, Northumbria University. from Northumbria
564 Research Link: http://nrl.northumbria.ac.uk/id/eprint/44081, 2020.

565 Hébert, A.-J., Flamand, A., and Chaillou, G.: Origins and transformations of terrigenous dissolved organic
566 matter in a transgressive coastal system, Estuar. Coast. Shelf S., 279, 108137,
567 https://doi.org/10.1016/J.ECSS.2022.108137, 2022.

568 Hedges, J. I., and Keil, R. G.: Sedimentary organic matter preservation: an assessment and speculative
569 synthesis, Mar. Chem., 49, 81–115, https://doi.org/10.1016/0304-4203(95)00008-F, 1995.

570 Helms, J. R., Stubbins, A., Ritchie, J. D., Minor, E. C., Kieber, D. J., and Mopper, K.: Absorption spectral
571 slopes and slope ratios as indicators of molecular weight, source, and photobleaching of chromophoric dissolved
572 organic matter, Limnol. Oceanogr., 53, 955–969, https://doi.org/10.4319/LO.2008.53.3.0955, 2008.

573 Holmes, R.M., McClelland, J.W., Peterson, B.J. *et al.* Seasonal and Annual Fluxes of Nutrients and Organic
574 Matter from Large Rivers to the Arctic Ocean and Surrounding Seas. Estuaries and Coasts, 35, 369–382,
575 https://doi.org/10.1007/s12237-011-9386-6, 2012.

576 Huguet, A., Vacher, L., Relexans, S., Saubusse, S., Froidefond, J.-M., and Parlanti, E.: Properties of fluorescent
577 dissolved organic matter in the Gironde Estuary, Org. Geochem., 40, 706–719,
578 https://doi.org/10.1016/j.orggeochem.2009.03.002, 2009.

579 Jones, B. M., Irrgang, A. M., Farquharson, L. M., Lantuit, H., Whalen, D., Ogorodov, S., Grigoriev, M.,
580 Tweedie, C., Gibbs, A. E., Strzelecki, M. C., Baranskaya, A., Belova, N., Sinitsyn, A., Kroon, A., Maslakov,
581 A., Vieira, G., Grosse, G., Overduin, P., Nitze, I., Maio, C., Overbeck, J., Bendixen, M., Zagórski, P., and
582 Romanovsky, V. E.: Arctic Report Card 2020: Coastal Permafrost Erosion, https://doi.org/10.25923/e47w-
583 dw52, 2020.

584 Kaiser, K., Benner, R., and Amon, R. M. W.: The fate of terrigenous dissolved organic carbon on the Eurasian
585 shelves and export to the North Atlantic, J. Geophys. Res.-Oceans, 122, 4–22,
586 https://doi.org/10.1002/2016jc012380, 2017a.

587 Kaiser, K., Canedo-Oropeza, M., McMahon, R., and Amon, R. M. W.: Origins and transformations of dissolved
588 organic matter in large Arctic rivers, Sci. Rep., 7, https://doi.org/10.1038/s41598-017-12729-1, 2017b.

589 Kipp, L. E., Charette, M. A., Moore, W. S., Henderson, P. B., and Rigor, I. G.: Increased fluxes of shelf-derived
590 materials to the central arctic ocean, Sci. Adv., 4, https://doi.org/10.1126/SCIADV.AAO1302, 2018.

591 Kipp, L. E., Chaillou, G., Kienast, M., Tamborski, J., and Whalen, D. : Radon and radium isotope signatures
592 on a massive ice- and permafrost-rich coastline, Geochimica et Cosmochimica Acta,
593 https://doi.org/10.1016/j.gca.2025.06.014, 2025.

594 Kwasigroch, U., Bełdowska, M., Jędruch, A., and Saniewska, D.: Coastal erosion—a "new" land-based source
595 of labile mercury to the marine environment, Environ. Sci. Pollut. Res., 25, 28682–28694,
596 https://doi.org/10.1007/S11356-018-2856-7, 2018.

597 Lalonde, K., Mucci, A., Ouellet, A., Gélinas, Y. : Preservation of organic matter in sediments promoted by iron.
598 Nature 483, 198–200. http://dx.doi.org/10.1038/nature10855, 2012.

599 Lantuit, H., Overduin, P. P., Couture, N., Wetterich, S., Aré, F., Atkinson, D., Brown, J., Cherkashov, G.,
600 Drozdov, D., Donald Forbes, L., Graves-Gaylord, A., Grigoriev, M., Hubberten, H. W., Jordan, J., Jorgenson,
601 T., Ødegård, R. S., Ogorodov, S., Pollard, W. H., Rachold, V., Sedenko, S., Solomon, S., Steenhuisen, F.,
602 Streletskaya, I., and Vasiliev, A.: The Arctic Coastal Dynamics Database: A New Classification Scheme and
603 Statistics on Arctic Permafrost Coastlines, Estuaries Coasts, 35, 383–400, https://doi.org/10.1007/S12237-010-
604 9362-6, 2012.

Lapham, L. L, Dallimore, S. R., Magen, C.,Henderson, L.C., Powers, L. C., Gonsior, M., Clark, B., Côté, M., Fraser, P., and Orcutt, B. N: MicrobialGreenhouse Gas DynamicsAssociated With Warming CoastalPermafrost, Western Canadian Arctic.Front. Earth Sci. 8:582103. https://doi.org/10.3389/feart.2020.582103, 2020.

Lecher, A.L.: Groundwater Discharge in the Arctic: A Review of Studies and Implications for Biogeochemistry, Hydrol. ,4(3),41, https://doi.org/10.3390/hydrology4030041, 2017.

Li, Q., Hu, W., Li, L., and Li, Y.: Interactions between organic matter and Fe oxides at soil micro-interfaces: Quantification, associations, and influencing factors, Sci. Total Environ., 855, https://doi.org/10.1016/j.scitotenv.2023.158710, 2023.

Linkhorst, A., Dittmar, T., and Waska, H.: Molecular Fractionation of Dissolved Organic Matter in a Shallow Subterranean Estuary: The Role of the Iron Curtain, Environ. Sci. Technol., 51, 1312–1320, https://doi.org/10.1021/acs.est.6b03608, 2017.

Lizotte, M., Juhls, B., Matsuoka, A., Massicotte, P., Mével, G., Anikina, D. O. J., Antonova, S., Bécu, G., Béguin, M., Bélanger, S., Bossé-Demers, T., Bröder, L., Bruyant, F., Chaillou, G., Comte, J., Couture, R.-M., Devred, E., Deslongchamps, G., Dezutter, T., Dillon, M., Doxaran, D., Flamand, A., Fell, F., Ferland, J., Forget, M.-H., Fritz, M., Gordon, T. J., Guilmette, C., Hilborn, A., Hussherr, R., Irish, C., Joux, F., Kipp, L., Laberge-Carignan, A., Lantuit, H., Leymarie, E., Mannino, A., Maury, J., Overduin, P., Oziel, L., Stedmon, C., Thomas, C., Tisserand, L., Tremblay, J.-É., Vonk, J., Whalen, D., and Babin, M.: Nunataryuk field campaigns: Understanding the origin and fate of terrestrial organic matter in the coastal waters of the Mackenzie Delta region, Earth Syst. Sci. Data, 15, 1617–1653, https://doi.org/10.5194/essd-2022-163, 2023.

Macdonald, R. W., Solomon, S. M., Cranston, R. E., Welch, H. E., Yunker, M. B., and Gobeil, C.: A sediment and organic carbon budget for the Canadian Beaufort Shelf, Mar. Geol., 144, 255–273, https://doi.org/10.1016/S0025-3227(97)00106-0, 1998.

628 Mackay, J.R.: Fifty years (1935-1985) of coastal retreat west of Tuktoyaktuk, District of Mackenzie, Geological
629 Survey of Canada, 86-1A, 727–735, 1986.

630 Massicotte, P., Asmala, E., Stedmon, C., and Markager, S.: Global distribution of dissolved organic matter
631 along the aquatic continuum: Across rivers, lakes and oceans, Sci. Total Environ., 609, 180–191,
632 https://doi.org/10.1016/j.scitotenv.2017.07.076, 2017.

633 Matsuoka, A., Bricaud, A., Benner, R., Para, J., Sempéré, R., Prieur, L., Bélanger, S., and Babin, M.: Tracing
634 the transport of colored dissolved organic matter in water masses of the Southern Beaufort Sea: relationship
635 with hydrographic characteristics, Biogeosciences, 9, 925–940, https://doi.org/10.5194/bg-9-925-2012, 2012.

636 Mehra, O.P., Jackson, M.L., : Iron oxide removal from soils and clays by a dithionitecitrate system buffered
637 with sodium bicarbonate. Clay Clay Miner. 7, 317–327, 1960.

638 McKnight, D. M., Boyer, E. W., Westerhoff, P. K., Doran, P. T., Kulbe, T., and Andersen, D. T.:
639 Spectrofluorometric characterization of dissolved organic matter for indication of precursor organic material
640 and aromaticity, Limnol. Oceanogr., 46, 38–48, https://doi.org/10.4319/lo.2001.46.1.0038, 2001.

641 McMeans, B. C., McCann, K. S., Humphries, M., Rooney, N., and Fisk, A. T.: Food Web Structure in
642 Temporally-Forced Ecosystems, Trends Ecol. Evol., 30, 662–672,
643 https://doi.org/10.1016/J.TREE.2015.09.001, 2015.

644 Meilleur, C., Kamula, M., Kuzyk, Z. A., and Guéguen, C.: Insights into surface circulation and mixing in James
645 Bay and Hudson Bay from dissolved organic matter optical properties, J. Mar. Syst., 238, 103841,
646 https://doi.org/10.1016/J.JMARSYS.2022.103841, 2023.

647 Moore, W. S.: The subterranean estuary: a reaction zone of ground water and sea water, Mar. Chem., 65(1–2),
648 111–125, doi:10.1016/S0304-4203(99)00014-6, 1999.

649 Moore, W. S., Benitez-Nelson, C., Schutte, C., Moody, A., Shiller, A., Sibert, R. J., and Joye, S.: SGD-OD:
650 investigating the potential oxygen demand of submarine groundwater discharge in coastal systems, Sci. Rep.,
651 14, 9249, https://doi.org/10.1038/s41598-024-59229-7, 2024.

652 Murphy, K. R., Stedmon, C. A., Graeber, D., and Bro, R.: Fluorescence spectroscopy and multi-way techniques.
653 PARAFAC, Anal. Methods, 5, https://doi.org/10.1039/c3ay41160e, 2013.

654 Nelson, N. B., Siegel, D. A., and Michaels, A. F.: Seasonal dynamics of colored dissolved material in the
655 Sargasso Sea, Deep Sea Res. Part I Oceanogr. Res. Pap., 45, 931–957, https://doi.org/10.1016/S0967-
656 0637(97)00106-4, 1998.

657 Nelson, N. B., and Siegel, D. A.: The global distribution and dynamics of chromophoric dissolved organic
658 matter, Annu. Rev. Mar. Sci., 5, 447–476, https://doi.org/10.1146/annurev-marine-120710-100751, 2013.

659 Nguyen, H. T., Lee, Y. M., Hong, J. K., Chen, M., and Hur, J. : Climate warming-driven changes in the flux of
660 dissolved organic matter and its effects on bacterial communities in the Arctic Ocean: A review. Frontiers
661 Marine Sciences. 9, 968583. https:// doi.org/ 10.3389/fmars.2022.968583, 2022.

662 Obu, J., Westermann, S., Bartsch, A., Berdnikov, N., Christiansen, H. H., Dashtseren, A., Delaloye, R.,
663 Elberling, B., Etzelmüller, B., Kholodov, A., Khomutov, A., Kääb, A., Leibman, M. O., Lewkowicz, A. G.,
664 Panda, S. K., Romanovsky, V., Way, R. G., Westergaard-Nielsen, A., Wu, T., Yamkhin, J., and Zou, D.:
665 Northern Hemisphere permafrost map based on TTOP modelling for 2000–2016 at 1 km² scale, Earth-Sci.
666 Rev., 193, 299–316, https://doi.org/10.1016/j.earscirev.2019.04.023, 2019.

667 Ohno, T.: Fluorescence Inner-Filtering Correction for Determining the Humification Index of Dissolved
668 Organic Matter, Environ. Sci. Technol., 36 (4), 742–746, https://doi.org/10.1021/es0155276, 2002.

669 Ouellette, D. S.: Thermal and Mechanical Modeling of Coastal Erosion Processes on Tuktoyaktuk Island,
670 Northwest Territories, Master thesis, University of Calgary, Calgary, Canada, 2021.

671 Pucher, M., Wünsch, U., Weigelhofer, G., Murphy, K., Hein, T., and Graeber, D.: staRdom: Versatile Software
672 for Analyzing Spectroscopic Data of Dissolved Organic Matter in R, Water, 11, 2366,
673 https://doi.org/10.3390/w11112366, 2019.

674 Riedel, T., Zak, D., Biester, H., and Dittmar, T.: Iron traps terrestrially derived dissolved organic matter at redox
675 interfaces, PNAS, 110, 10101–10105, https://doi.org/10.1073/pnas.1221487110, 2013.

676 Santos, I. R., Eyre, B. R., Huettel, M.: The driving forces of porewater and groundwater flow in permeable
677 coastal sediments: A review, Estuarine, Coastal and Shelf Science : 98, 1-
678 15,https://doi.org/10.1016/j.ecss.2011.10.024, 2012.

679 Schuur, E. A. G., McGuire, A. D., Schädel, C., Grosse, G., Harden, J. W., Hayes, D. J., Hugelius, G., Koven,
680 C. D., Kuhry, P., Lawrence, D. M., Natali, S. M., Olefeldt, D., Romanovsky, V. E., Schaefer, K., Turetsky, M.
681 R., Treat, C. C., and Vonk, J. E.: Climate change and the permafrost carbon feedback, Nature, 520, 171–179,
682 https://doi.org/10.1038/nature14338, 2015.

683 Sirois, M., Couturier, M., Barber, A., Gélinas, Y., and Chaillou, G.: Interactions between iron and organic
684 carbon in a sandy beach subterranean estuary, Mar. Chem., 202, 86–96,
685 https://doi.org/10.1016/j.marchem.2018.02.004, 2018.

686 Solomon, S. M.: Spatial and temporal variability of shoreline change in the Beaufort-Mackenzie region,
687 northwest territories, Canada, Geo-Mar. Lett., 25, 127–137, https://doi.org/10.1007/S00367-004-0194-X, 2005.

688 Spencer, R. G., Aiken, G. R., Dornblaser, M. M., Butler, K. D., Holmes, R. M., Fiske, G., and Stubbins, A.:
689 Chromophoric dissolved organic matter export from US rivers, Geophys. Res. Lett., 40, 1575–1579,
690 https://doi.org/10.1002/grl.50357, 2013.

691 Stedmon, C. A., Amon, R. M. W., Rinehart, A. J., and Walker, S. A.: The supply and characteristics of colored
692 dissolved organic matter (CDOM) in the Arctic Ocean: Pan Arctic trends and differences, Mar. Chem., 124,
693 108–118, https://doi.org/10.1016/j.marchem.2010.12.007, 2011.

694 Stedmon, C. A., Markager, S., and Bro, R.: Tracing dissolved organic matter in aquatic environments using a
695 new approach to fluorescence spectroscopy, Mar. Chem., 82, 239–254, https://doi.org/10.1016/s0304-
696 4203(03)00072-0, 2003.

697 Stookey, L. L.: Ferrozine—A New Spectrophotometric Reagent for Iron, Anal. Chem., 42, 779–781,
698 https://doi.org/10.1021/AC60289A016, 1970.

699 Tanguy, R., Whalen, D., Prates, G., and Vieira, G.: Shoreline change rates and land to sea sediment and soil
700 organic carbon transfer in eastern Parry Peninsula from 1965 to 2020 (Amundsen Gulf, Canada), Arctic Sci.,
701 1–20, https://doi.org/10.1139/as-2022-0028, 2023.

702 Tanski, G., Wagner, D., Knoblauch, C., Fritz, M., Sachs, T., and Lantuit, H.: Rapid CO2 release from eroding
703 permafrost in seawater. Geophysical Research Letters, 46, 11244–11252.
704 https://doi.org/10.1029/2019GL084303, 2019.

705 Terhaar, J., Lauerwald, R., Regnier, P. *et al.* Around one third of current Arctic Ocean primary production
706 sustained by rivers and coastal erosion. Natuew Communications, 12, 169. https://doi.org/10.1038/s41467-020-
707 20470-z, 2021

708 Thingstad, T. F., Bellerby, R. G. J., Bratbak, G., Børsheim, K. Y., Egge, J. K., Heldal, M., Larsen, A., Neill,
709 C., Nejstgaard, J., Norland, S., Sandaa, R. A., Skjoldal, E. F., Tanaka, T., Thyrhaug, R., and Töpper, B.:
710 Counterintuitive carbon-to-nutrient coupling in an Arctic pelagic ecosystem, Nature, 455, 387–390,
711 https://doi.org/10.1038/nature07235, 2008.

712 Utting, N., Clark, I., Lauriol, B., Wieser, M., and Aeschbach-Hertig, W.: Origin and Flow Dynamics of
713 Perennial Groundwater in Continuous Permafrost Terrain using Isotopes and Noble Gases: Case Study of the
714 Fishing Branch River, Northern Yukon, Canada, Permafrost Periglac., 23, 91–106,
715 https://doi.org/10.1002/ppp.1732, 2012.

716 Viollier, E., Inglett, P. W., Hunter, K., Roychoudhury, A. N., and Van Cappellen, P.: The ferrozine method
717 revisited: Fe(II)/Fe(III) determination in natural waters, Appl. Geochem., 15, 785–790,
718 https://doi.org/10.1016/S0883-2927(99)00097-9, 2000.

719 Vonk, J. E., Semiletov, I. P., Dudarev, O. V., Eglinton, T. I., Andersson, A., Shakhova, N., Charkin, A., Heim,
720 B., and Gustafsson, Ö.: Preferential burial of permafrost-derived organic carbon in Siberian-Arctic shelf waters,
721 J. Geophys. Res.: Oceans, 119, 8410–8421, https://doi.org/10.1002/2014JC010261, 2014.

722 Vonk, J. E., Tank, S. E., Bowden, W. B., Laurion, I., Vincent, W. F., Alekseychik, P., Amyot, M., Billet, M.
723 F., Canário, J., Cory, R. M., Deshpande, B. N., Helbig, M., Jammet, M., Karlsson, J., Larouche, J.,
724 Macmillan, G., Rautio, M., Walter Anthony, K. M., and Wickland, K. P.: Reviews and syntheses: Effects of
725 permafrost thaw on Arctic aquatic ecosystems, Biogeosciences, 12, 7129–7167, https://doi.org/10.5194/bg-
726 12-7129-2015, 2015.

727 Vonk, J. E., Fritz, M., Speetjens, N. J. et al. : The land–ocean Arctic carbon cycle. Nature Reviews Earth
728 Environment 6, 86–105, https://doi.org/10.1038/s43017-024-00627-w, 2025.

729 Walvoord, M. A., and Striegl, R. G.: Increased groundwater to stream discharge from permafrost thawing in
730 the Yukon River basin: Potential impacts on lateral export of carbon and nitrogen, Geophys. Res. Lett., 34,
731 https://doi.org/10.1029/2007gl030216, 2007.

732 Waska, H., Simon, H., Ahmerkamp, S., Greskowiak, J., Ahrens, J., Seibert, S. L., Schwalfenberg, K., Zielinski,
733 O., and Dittmar, T.: Molecular traits of dissolved organic matter in the subterranean estuary of a high-energy
734 beach: Indications of sources and sinks, Front. Mar. Sci., 8, 54,
735 https://doi.org/10.3389/FMARS.2021.607083/BIBTEX, 2021.

736 Weishaar, J. L., Aiken, G. R., Bergamaschi, B. A., Fram, M. S., Fujii, R., and Mopper, K.: Evaluation of
737 specific ultraviolet absorbance as an indicator of the chemical composition and reactivity of dissolved organic
738 carbon, Environ. Sci. Technol., 37, 4702–4708, https://doi.org/10.1021/es030360x, 2003.

739 Whalen, D., Forbes, D. L., Kostylev, V., Lim, M., Fraser, P., Nedimović, M. R., and Stuckey, S.: Mechanisms,
740 volumetric assessment, and prognosis for rapid coastal erosion of Tuktoyaktuk Island, an important natural
741 barrier for the harbour and community, Can. J. Earth Sci., 59, 945–960, https://doi.org/10.1139/cjes-2021-0101,
742 2022.

743 Wurl, O., and Tsai, M. S.: Analysis of Dissolved and Particulate Organic Carbon with the HTCO Technique,
744 in: Practical Guidelines for the Analysis of Seawater, CRC Press, pp. 45–60, 2009.

745 Zhou, Z., Henkel, S., Kasten, S., and Holtappels, M.: The iron “redox battery” in sandy sediments: Its impact
746 on organic matter remineralization and phosphorus cycling. Sci. Total. Environ., 865, 161168,
747 https://doi.org/10.1016/j.scitotenv.2022.161168., 2023.

748 Zhou, Z., Waska, H., Henkel, S., Dittmar, T., Kasten, S., and Holtappels, M.: Iron promotes the retention of
749 terrigenous Dissolved organic matter in subtidal Permeable Sediments. Environ. Sci. Technol., 58,
750 6204−6214, https://doi.org/10.1021/acs.est.3c09531, 2024.

751

752 **TABLES**

753 Table 1 : Description of the EEM-PARAFAC modelled FDOM components based on the literature results of

754 literature references. PARAFAC components and their characteristics

Comp.	Peak max Ex/Em	Coble peak	Description	Literature
C1	250-335/466	A, C	Humic-like terrestrial, HMW, aromatic	C_C : <240-340/452 (Olefeldt et al., 2014) ALL1: 250-350/459 (Pitta and Zeri 2021) C3: <240-355/476 (Stedmon and Markager, 2005a) C3: 260-370/490 (Murphy et al., 2018) C4: <255-360/460 (Fouché et al., 2020)
C2	265/296	B	Protein-like, tyrosine, biological, microbial autochthonous origin. LMW phenolic compounds.	C_{Ty}: 270/<300 (Olefeldt et al., 2014) ACT-10 C3: 270/302 (D'Andrilli and McConnell 2021) C6: 280/338 (Stedmon and Markager, 2005a) C1:275/<300 (Murphy et al. 2008) C1: 275/306 (Fouché et al., 2020)
C3	250-295/414	A, M	Humic-like, terrestrial, autochtonous production and microbial processing, LMW.	C_M :<240,305/404 (Olefeldt, Persson et al. 2014) C2: <300/396 (Søndergaard, Stedmon et al. 2003) C2 : 315/418 (Murphy et al., 2008) C2: 310/ 415 (Fouché et al., 2020)

755

756

757 Table 2 : Particulate fraction characteristics of sandy beach sediment collected at Tuktoyaktuk Island and

758 Peninsula Point.

	Tuktoyaktuk Island N=3	Peninsula Point N=2
Sediment depth layer (cm)	0-50	0-30
Total organic carbon (% dry sediment)	0.43 ± 0.12	0.21 ± 0.07
Reactive sediment Fe (ppm; µg Fe/g dry sediment)	2,246 ± 0,850	1,320± 0,250

759

760

761

FIGURE CAPTIONS

Fig. 1 Map of the four sampling sites (red dots) located in the Northwest Territories, Canada.

Fig. 2 Schematic cross-sections and photographs illustrating the permafrost–seawater continuum landscape at Tuktoyaktuk Island (A) and Peninsula Point (B; not to scale). Black arrows indicate surface (solid lines) and subsurface (dashed lines) theoretical flow paths, while blue arrows represent recirculating seawater driven by tide and wave inputs into the sandy beaches. These conceptual models are adapted from Kipp et al. (2025) based on Hayes et al. (2022) for Peninsula Point and Whalen et al. (2022) and Warren et al. (2025) for Tuktoyaktuk Island.

Fig. 3 Excitation-emission matrix (EEM) fluorescence spectra of the 3-component PARAFAC model. Fluorescence is expressed in Raman Unit (R.U.).

Fig. 4 Isotopic composition of massive ice, meltwater, beach groundwater and seawater samples collected in 2019 showing the mixing line between samples across the salinity gradient, from the meltwater to the seawater. The global meteoric water line (GMWL; Craig, 1961) and the local meteoric water line for Inuvik (LMWL, Fritz et al., 2022) are also reported. Note that only one massive ice sample (N=1) was collected in 2019.

Fig. 5 Distribution of (A) DOC, (B) aCDOM350, (C) HIX, and (D) SUVA254 across the salinity gradient (S) and among the different sample types (i.e., beach groundwater, massive ice, meltwater, and seawater). Note that only one massive ice sample is included. The zoomed-in panels display only beach groundwater and seawater samples, along with a theoretical mixing line (dashed black line) connecting the “fresh” and “salty” endmembers. These endmembers were defined based on the most enriched and depleted stable isotope signatures in the dataset, corresponding to salinity values of 20.08 (N = 1) and 0.18-0.30 (N = 8), respectively. In the boxplots, black lines indicate the medians, whiskers represent the full range of data, and individual points denote outliers.

Fig. 6 Global relationship between absorption coefficients at 350 nm (aCDOM350 in m^{-1}) and DOC concentrations (in µmol L^{-1}) along the permafrost to nearshore aquatic continuum. Note that the data is reported in Log units.

Fig. 7 Distribution of total dissolved Fe (Fe_{tot}, µmol L^{-1}) (A), and Fe-DOC ratio (B) across the salinity gradient (S), and by sample type. The y-axis in each panel is shown on a logarithmic scale to accommodate the broad range of Fe concentrations.

Fig. 8 Behaviour of (A) DOC and (B) aCDOM350 concentrations with excess iron and constant oxygenation in the different types of collected samples incubated over 48 hours. The non-colored points indicate the concentrations before the Fe addition at t=0h.

Fig. 9 Distribution of PARAFAC components (A) C1, (B) C2, and (C) C3 along the salinity gradient (S) and for the different types of collected samples (*i.e.,* beach groundwater, massive ice, meltwater and nearshore seawater samples). Note that only one massive ice sample is reported here. For the boxplots, the black lines represent the median values, the whiskers represent the extent of the data, and the dot points represent the outlier values.

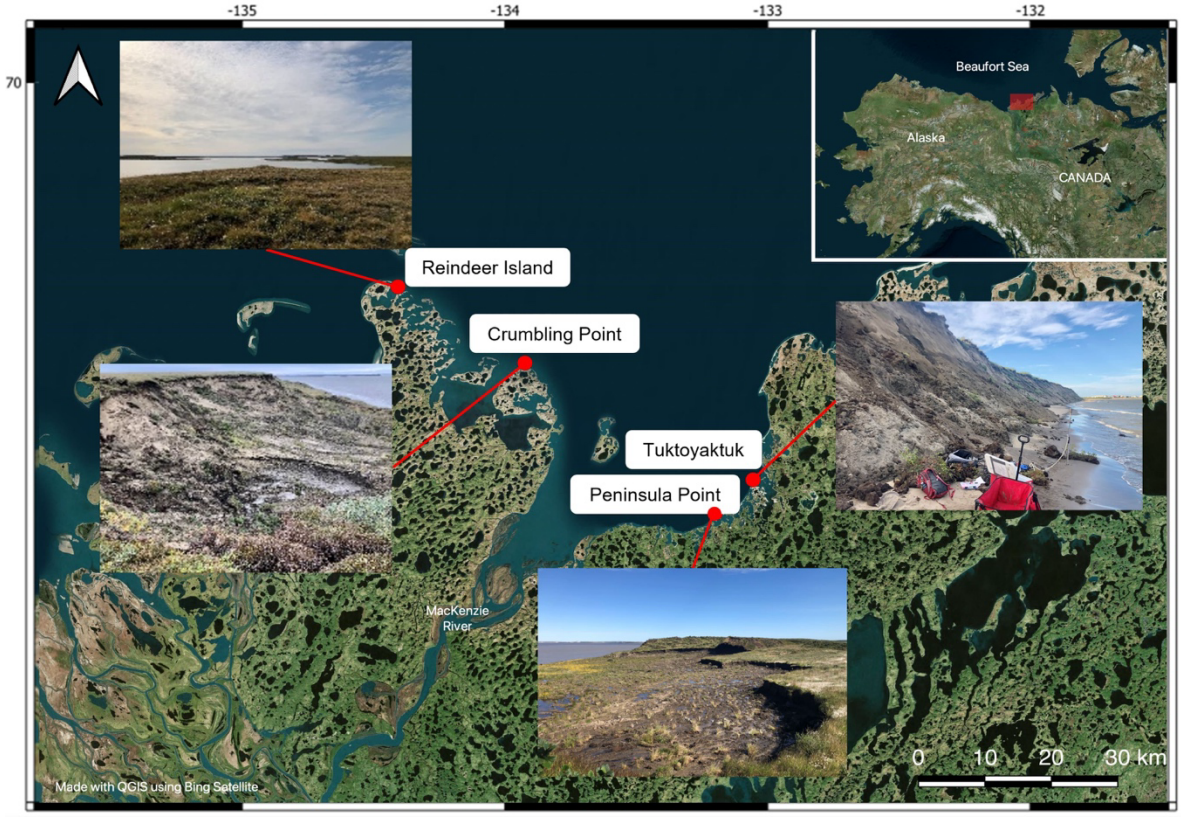

Fig. 1 Map of the four sampling sites (red dots) located in the Northwest Territories, Canada.

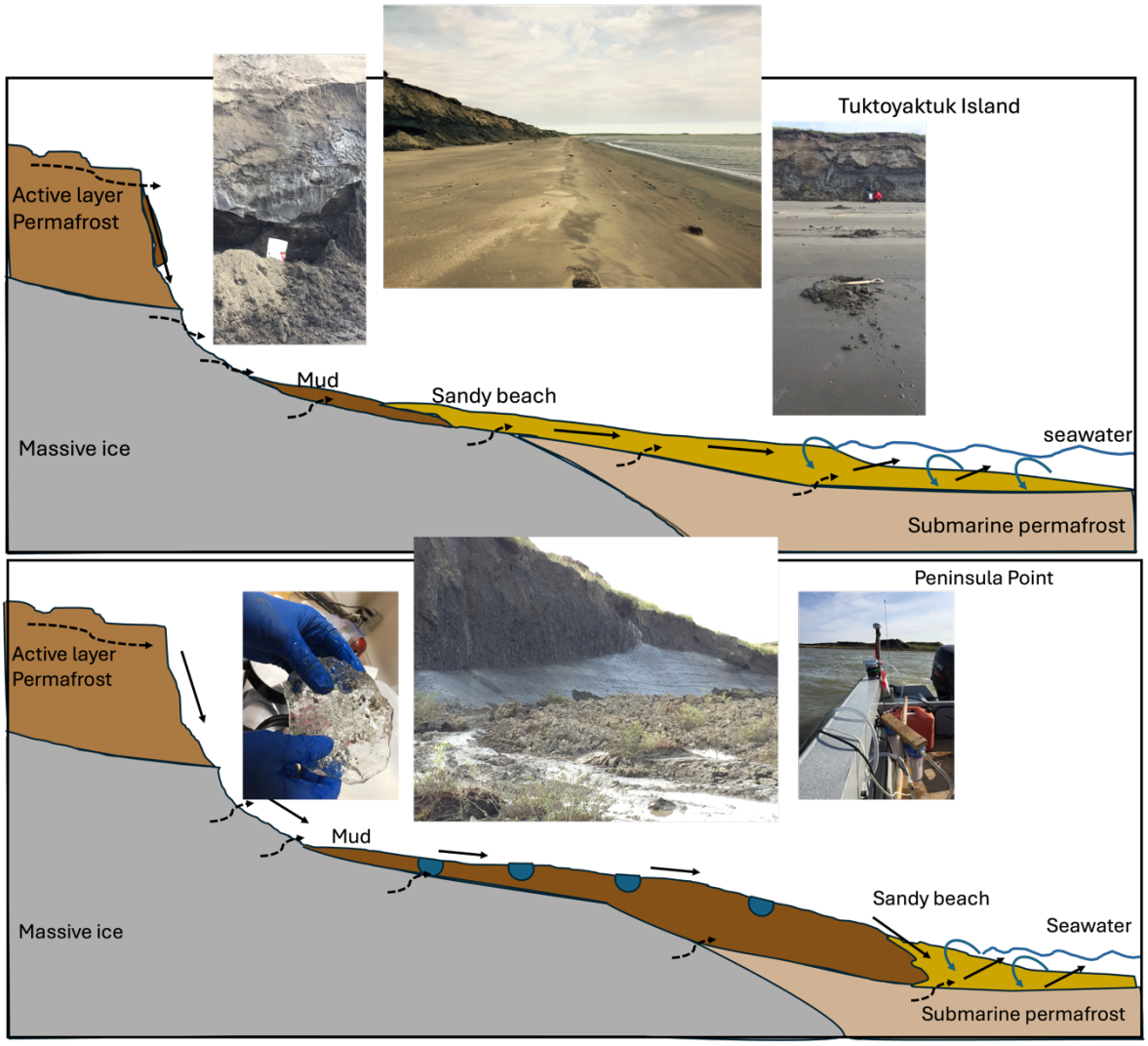

802

803 **Fig. 2** Schematic cross-sections and photographs illustrating the permafrost–seawater continuum landscape at
804 Tuktoyaktuk Island (A) and Peninsula Point (B; not to scale). Black arrows indicate surface (solid lines) and
805 subsurface (dashed lines) theoretical flow paths, while blue arrows represent recirculating seawater driven by
806 tide and wave inputs into the sandy beaches. These conceptual models are adapted from Kipp et al. (2025) based
807 on Hayes et al. (2022) for Peninsula Point and Whalen et al. (2022) and Warren et al. (2025) for Tuktoyaktuk
808 Island.

809

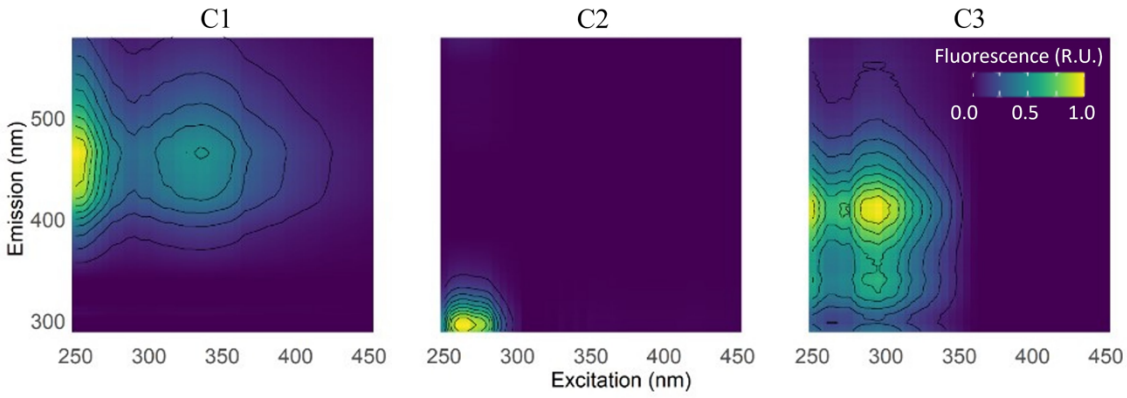

810

811 **Fig. 3** Excitation-emission matrix (EEM) fluorescence spectra of the 3-component PARAFAC model.

812 Fluorescence is expressed in Raman Unit (R.U.).

813

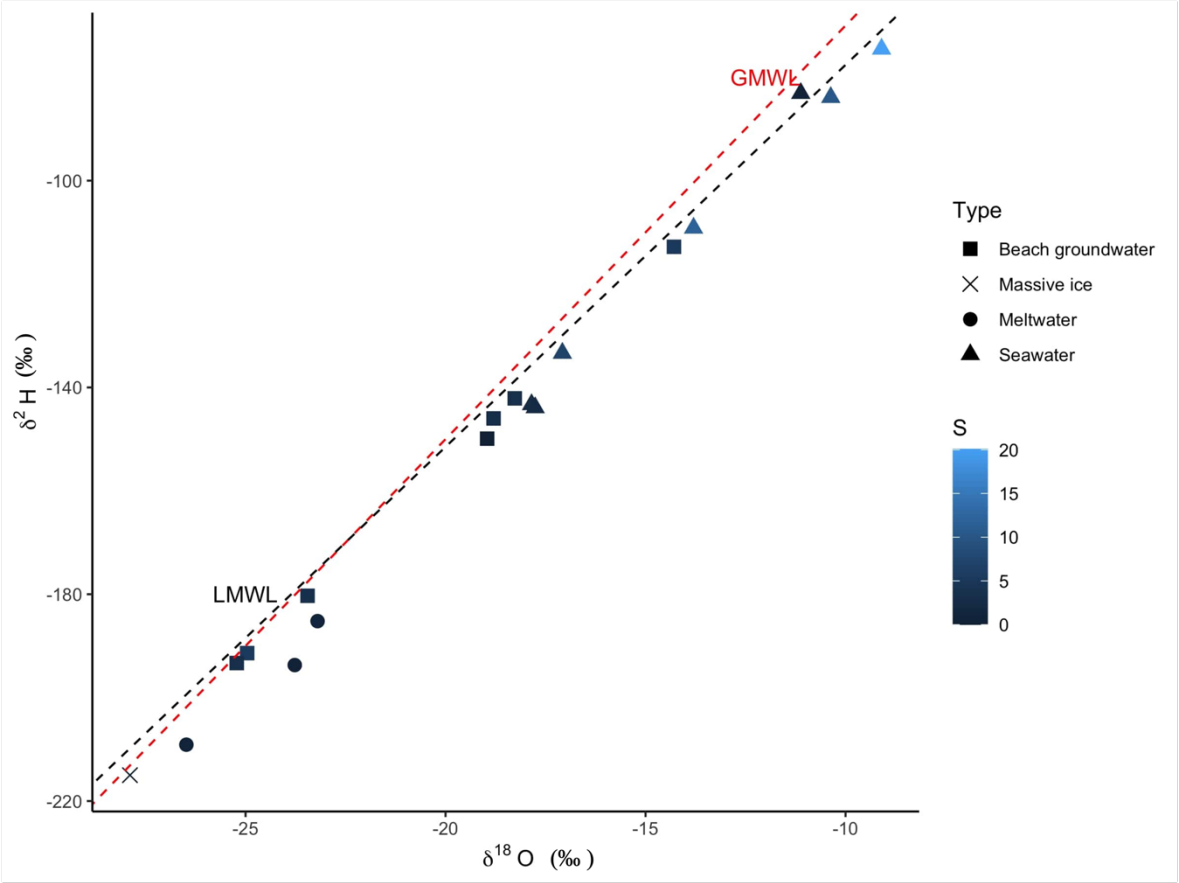

814

815 **Fig. 4** Isotopic composition of massive ice, meltwater, beach groundwater and seawater samples collected in

816 2019 showing the mixing line between samples across the salinity gradient, from the meltwater to the seawater.

817 The global meteoric water line (GMWL; Craig, 1961) and the local meteoric water line for Inuvik (LMWL,

818 Fritz et al., 2022) are also reported. Note that only one massive ice sample (N=1) was collected in 2019.

819

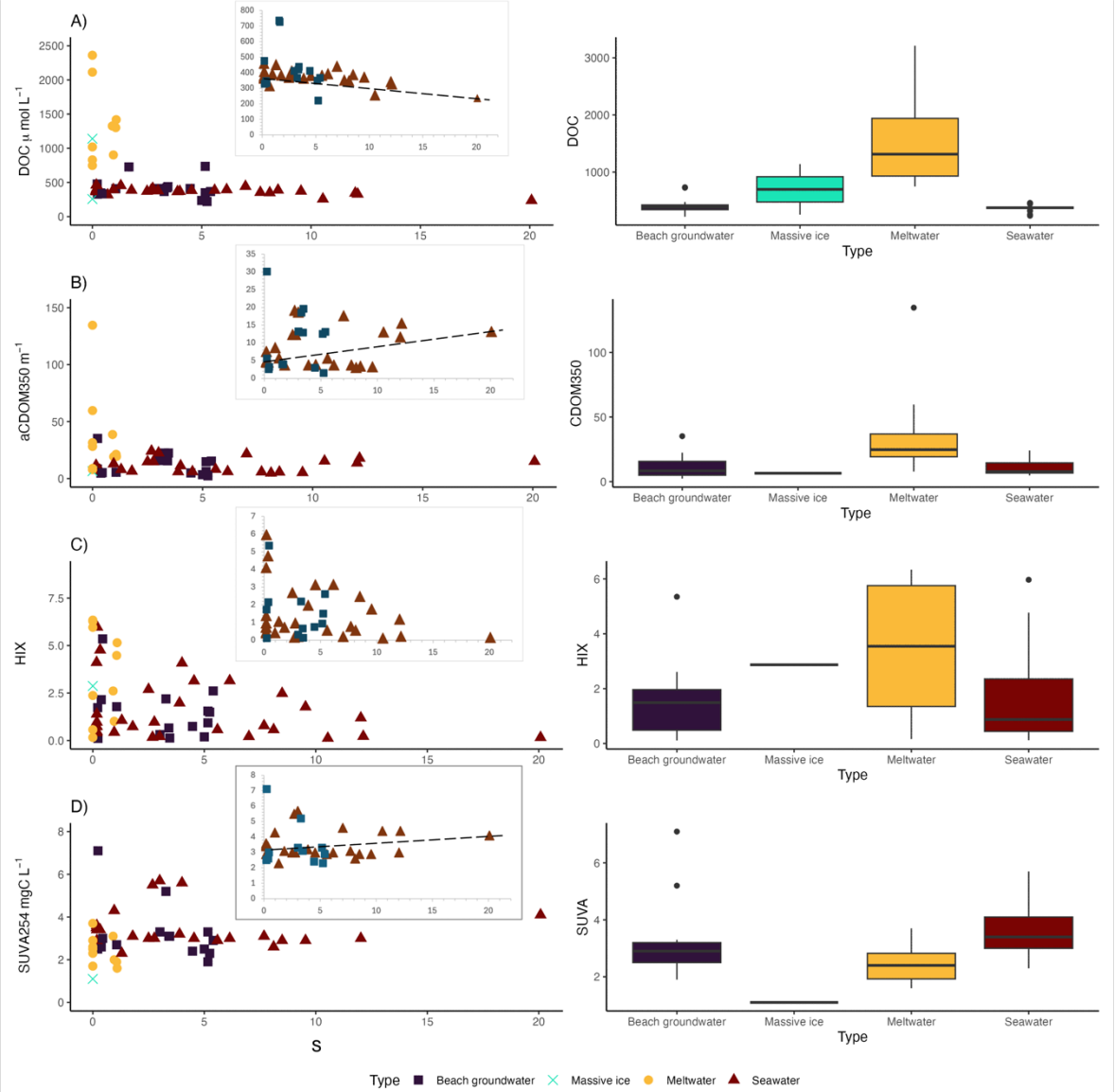

Fig. 5 Distribution of (A) DOC, (B) aCDOM350, (C) HIX, and (D) SUVA254 across the salinity gradient (S) and among the different sample types (i.e., beach groundwater, massive ice, meltwater, and seawater). Note that only one massive ice sample is included. The zoomed-in panels display only beach groundwater and seawater samples, along with a theoretical mixing line (dashed black line) connecting the "fresh" and "salty" endmembers. These endmembers were defined based on the most enriched and depleted stable isotope signatures in the dataset, corresponding to salinity values of 20.08 (N = 1) and 0.18-0.30 (N = 8), respectively. In the boxplots, black lines indicate the medians, whiskers represent the full range of data, and individual points denote outliers.

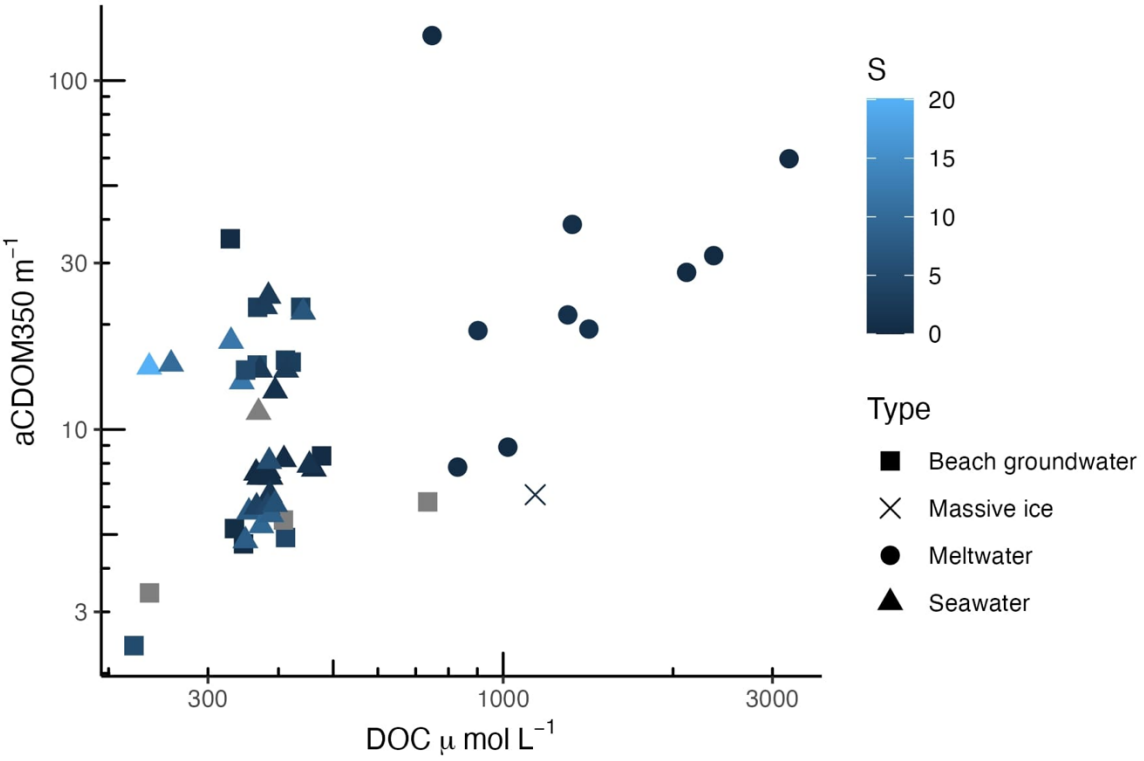

830

831 **Fig. 6** Global relationship between absorption coefficients at 350 nm (aCDOM350 in m^{-1}) and DOC

832 concentrations (in µmol L^{-1}) along the permafrost to nearshore aquatic continuum. Note that the data is

833 reported in Log units.

834

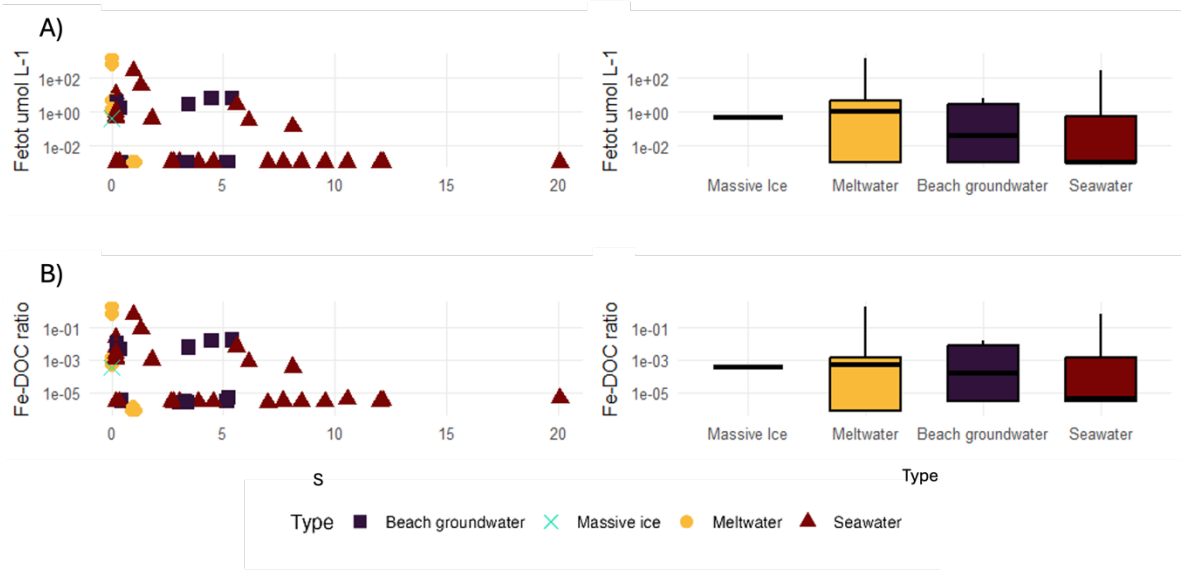

835

836 **Fig. 7** Distribution of total dissolved Fe (Fe_{tot}, µmol L^{-1}) (A), and Fe-DOC ratio (B) across the salinity gradient

837 (S), and by sample type. The y-axis in each panel is shown on a logarithmic scale to accommodate the broad

838 range of Fe concentrations.

839

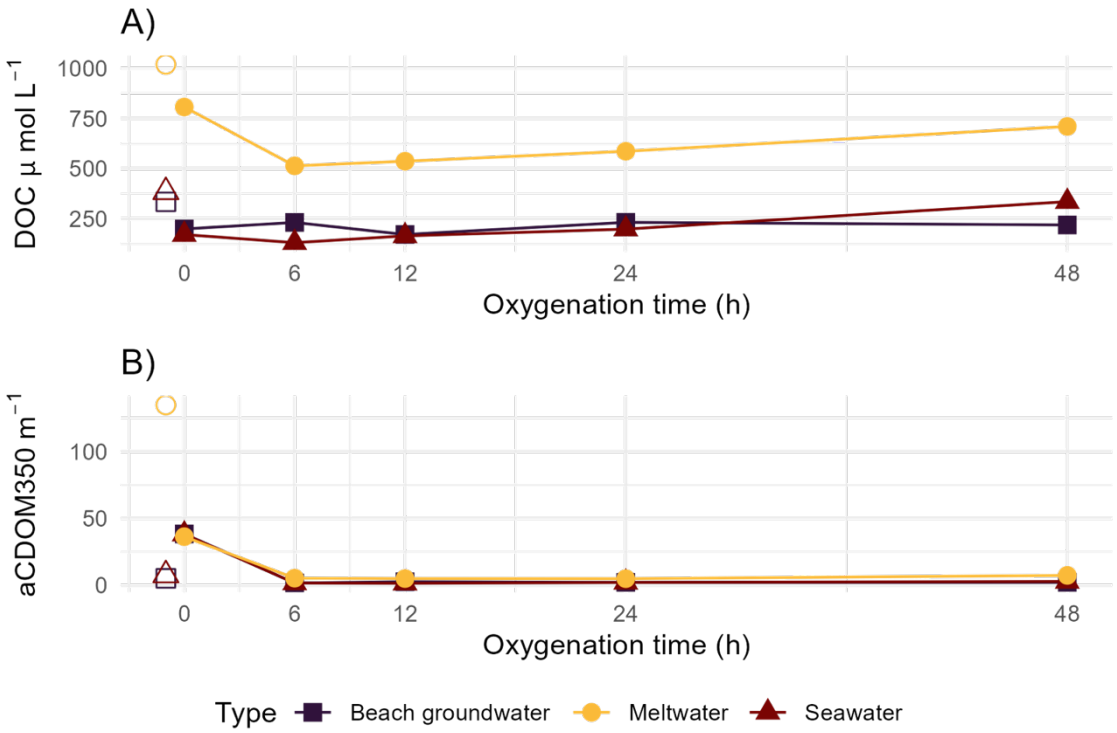

840

841 **Fig. 8** Behaviour of (A) DOC and (B) aCDOM350 concentrations with excess iron and constant oxygenation

842 in the different types of collected samples incubated over 48 hours. The non-colored points indicate the

843 concentrations before the Fe addition at t=0h.

844

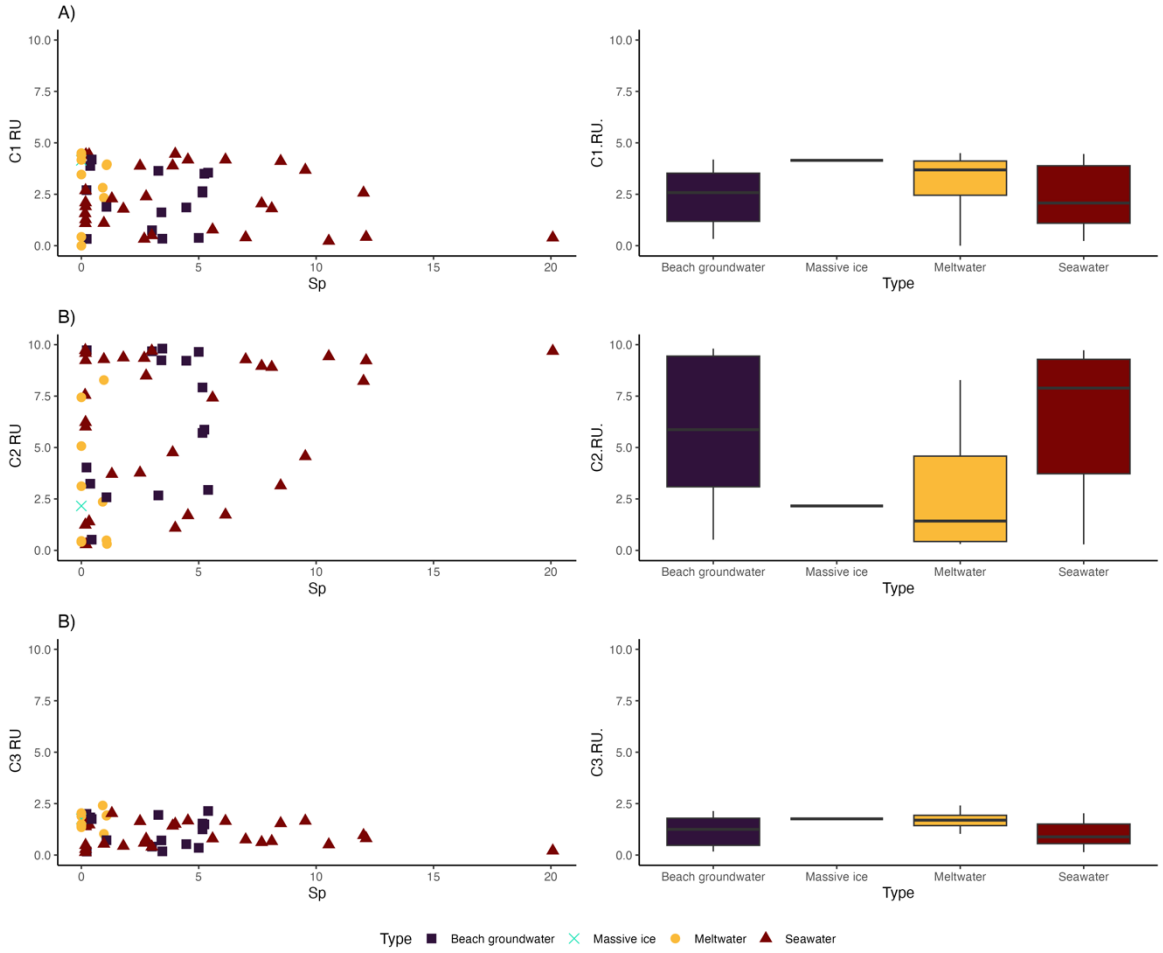

845

846 **Fig. 9** Distribution of PARAFAC components (A) C1, (B) C2, and (C) C3 along the salinity gradient (S) and
847 for the different types of collected samples (*i.e.,* beach groundwater, massive ice, meltwater and nearshore
848 seawater samples). Note that only one massive ice sample is reported here. For the boxplots, the black lines
849 represent the median values, the whiskers represent the extent of the data, and the dot points represent the
850 outlier values.

851